Chapter 6

Fiber Grating Band-pass Filters

Let the band pass. . . .

For many applications, the transmission characteristics of a fiber Bragg grating are really the wrong way around: it is a *band-stop* rather than a *band-pass* filter. For example, tuning a radio enables the *selection* of a channel, not the *rejection* of it from a broad frequency spectrum. However, a Bragg grating works quite in reverse, and therefore cannot be easily used for channel selection. Optical transmission systems also require a "channel-dropping" function, in which a channel is selected from a large spectrum of designated channels. These optical channels are on a coarse grid of 100 GHz (multiples and submultiples of), which is currently being debated. A system based on wavelength or frequency sliced channels is a logical one and will prevail in future telecommunications networks. The advantage of such a standardized system is not in doubt, only the allocation of the channels, which is a matter for discussion by international standards committees around the world. In view of the future worldwide integration of telecommunication services, it is only a matter of time before an industry standard emerges.

The immediate question that springs to mind is: Will fiber gratings play a role in emerging systems, given that their function is not the one naturally desired in a majority of application in filtering? The answer to

the question lies in their ability to invert the function to the desired one with a minimum of engineering and expense. The sales volume of gratings will crucially depend on how well and easily they fit this task. A problem needing a solution is ideal for creativity. To this end a number of options have appeared. None is ideal, but within the context of a wider technology, there are appropriate solutions for many applications, albeit at a cost.

What are the options? These may be categorized into two types. First are those that work in reflection, as is normally the case with Bragg gratings. These are principally the following:

1. The optical circulator with grating
2. The single grating in one arm of a coupler
3. (Possibly the most attractive) The in-coupler reflection band-pass filter
4. The dual grating Michelson interferometer
5. The dual grating Mach–Zehnder interferometer
6. The super-structure grating

Those that work in transmission include most notably:

7. The distributed feedback (DFB) grating
8. The Fabry–Perot interferometer
9. The composite moiré resonator
10. The chirped grating, or radiation loss with transmission window
11. The side-tap filter
12. The long-period copropagating radiation mode coupler
13. The polarization rocking coupler
14. The intermodal coupler
15. The in-coupler Bragg grating transmission filter

The above list may be subdivided into interferometric, which include devices 4–9, and noninterferometric. It is worth noting that although interferometric devices conjure up the image of sensitivity to external stimuli, it is not necessarily true of all in that category (devices 6, 7, and 9). By suitable design, devices 4, 5, and 8 have been rendered insensitive and demonstrated to be stable. All gratings are temperature and strain sensitive; however, the temperature sensitivity is low, <0.02 nm/°C, so that over a working temperature range of 100°C, the change in the op-

erating wavelength is only ~2 nm. As a fraction of the channel spacing (100 GHz or 0.8 nm), it is still too large and must be stabilized. Thus, schemes need to be developed to counter the effects of temperature. Passive packaging can isolate the grating from experiencing effects of strain. Both temperature and strain have been used along with grating-based band-pass filters to control novel functions such as optical add–drop multiplexers and demultiplexers.

We now consider some of these filters in detail, along with their attributes and shortcomings.

6.1 Distributed feedback, Fabry–Perot, superstructure, and moiré gratings

The general form of the band-pass filter described in this section is a grating or a combination of gratings physically written at the same location. The composite transmission spectrum of this band-pass filter can be a single or a series (one to many) of high transmission windows separated by bands that are rejected by reflection.

6.1.1 The distributed feedback grating

The distributed feedback fiber grating is probably the simplest band-pass filter and comprises a phase-step within the length of the grating. It is a Fabry–Perot filter with a gap of less than one Bragg wavelength. The position and the size of the phase step determine the position and the wavelength of transmission band. A schematic of this grating is shown in Fig. 6.1.

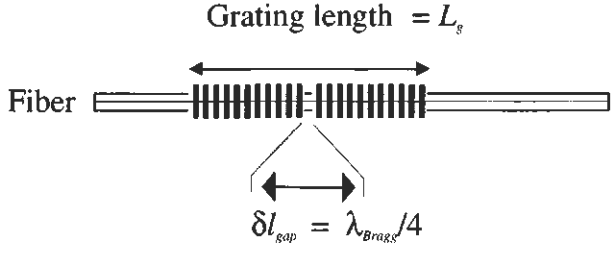

Figure 6.1: The fiber DFB Bragg grating. A transmission peak appears in the center of the band stop when the gap is precisely $\lambda/4$.

The DFB structure is used in semiconductor lasers to enable single frequency operation [1,2]. The single $\lambda/4$ phase-shifted DFB [1] has a pass band in the middle of the stop band. The pass band has a very narrow Lorentzian line shape. While this narrow pass band is useful for filtering, the need exists for broader-bandwidth, high-finesse transmission filters. Cascading several such structures leads to an improved, broader transmission bandwidth [3–5], and has been generally well known in electrical filter design. The developments in fiber Bragg grating technology have made it possible to fabricate direct in-fiber analogs. Low-loss, high-finesse filters, using both a single $\lambda/4$-shifted and cascaded phase-shifted DFB structures have been reported in the literature [6,7]. Rare-earth-doped fiber DFB lasers (see Chapter 8) have also been demonstrated [8].

Coupled-mode analysis developed in Chapter 4 leads directly to the fields in each grating. The matrix method provides a simple route to the transfer function of the DFB structure. Recalling Eq. (4.8.22), the transfer matrix of the DFB is

$$T_{DFB} = T^2 T^{ps} T^1, \tag{6.1.1}$$

where TP^s is the phase shift matrix shown in Eq. (4.8.19)

$$T^{ps} = \begin{bmatrix} e^{-i(\phi/2)} & 0 \\ 0 & e^{+i(\phi/2)} \end{bmatrix}. \tag{6.1.2}$$

Remembering that the transfer matrix elements of T^1 and T^2 are described by Eqs. (4.8.18)–(4.8.21) immediately leads to the solution for the DFB transfer function, T_{DFB}:

$$\begin{aligned} T^{DFB} &= \begin{bmatrix} T_{11}^2 T_{11}^1 T_{11}^{ps} + T_{12}^2 T_{21}^1 T_{22}^{ps} & T_{11}^2 T_{11}^1 T_{11}^{ps} + T_{12}^2 T_{22}^1 T_{22}^{ps} \\ T_{21}^2 T_{11}^1 T_{11}^{ps} + T_{22}^2 T_{21}^1 T_{22}^{ps} & T_{21}^2 T_{12}^1 T_{11}^{ps} + T_{22}^2 T_{22}^1 T_{22}^{ps} \end{bmatrix} \\ &= \begin{bmatrix} T_{11}^{DFB} & T_{12}^{DFB} \\ T_{21}^{DFB} & T_{22}^{DFB} \end{bmatrix}. \end{aligned} \tag{6.1.3}$$

The transmitted power according to Eq. (4.8.8) is

$$|\tau^{DFB}|^2 = \left| \frac{1}{T_{11}^{DFB}} \right|^2 = \frac{1}{T_{11}^{DFB}(T_{11}^{DFB})^*} = \left| \frac{1}{T_{11}^2 T_{11}^1 T_{11}^{ps} + T_{12}^2 T_{21}^1 T_{22}^{ps}} \right|^2, \tag{6.1.4}$$

where * indicates the complex conjugate, and $T_{22}^{ps} = (T_{11}^{ps})^*$.

From conservation of energy, we find that the reflectivity

$$|\rho^{DFB}|^2 = 1 - |\tau^{DFB}|^2. \tag{6.1.5}$$

Note that in general both grating sections need not be placed symmetrically around the phase step and that the gratings may have different bandwidths and refractive index modulation amplitudes. However, the simple band-pass filter has, in the center of a uniform grating, a $\pi/2$ phase step, which has the effect of introducing a single pass-band in the transmission spectrum. In this case, $T_{21}^1 = (T_{12}^2)^*$, and $T_{11}^1 = T_{11}^2$. Figure 6.2 shows the band-pass spectrum of two 3-mm-long gratings, each with a quarter-wavelength step in the center. The amplitudes of the refractive index modulation are 5×10^{-4} and 10^{-3}. Notice that although there is a very narrow transmission band in the center of the grating spectrum within a band stop of ~1 nm, there are strong side lobes on either side. The band pass is a highly selective filter within a relatively narrow band stop. A uniform grating of the same length but without the phase step has a bandwidth approximately half that of the full band stop of the DFB grating. The DFB grating may be viewed as being composed of two single gratings, each half the length of a uniform one.

The phase mask allows the replication of phase-shifted DFB structures into fibers in a simple and controlled manner [6]. This has been done successfully to produce a variety of band-pass DFB structures, and

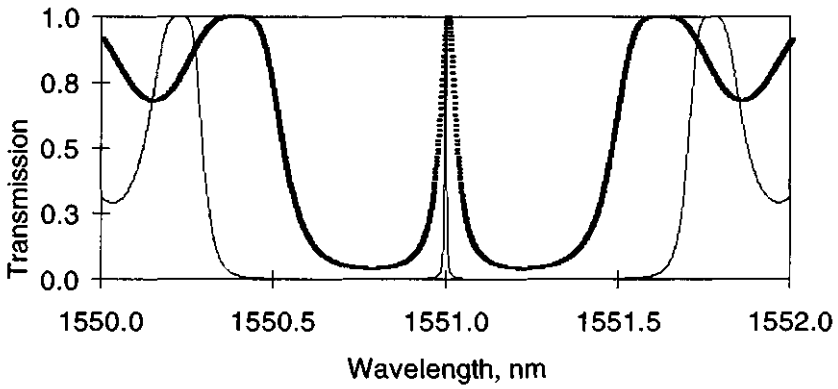

Figure 6.2: The calculated transmission spectrum of 3-mm-long DFB gratings, with a $\lambda/4$ phase-step and refractive index modulation 5×10^{-4} for the dashed line and 10^{-3} for the continuous line, respectively.

the transmission spectrum of one such grating is shown in Fig. 6.3. In this grating, a phase step of $\lambda/4$ was introduced in the middle of the phase mask and replicated. This type of grating is a simple Fabry–Perot interferometer that has a band stop inversely proportional to $\sim 0.25Lg$. A feature to note is the second peak on the side of the main band pass, which is due to the birefringence of the fiber estimated from the separation to be $\sim 1 \times 10^{-5}$. The combination of photoinduced and intrinsic birefringence becomes apparent with the extremely narrow band-pass structure of the DFB grating. The finesse of this DFB grating was ~67. The transmission peak is very sensitive to losses within the grating structure. Note that although the band pass has not been fully resolved, there is OH^- absorption loss in this grating because of hydrogenation, and consequently, the transmission peak is diminished.

Phase shifts within a grating can be produced in several ways. Canning and Sceats [7] showed that postprocessing the center of a uniform grating with UV radiation results in a permanent phase-shifted structure. This method relies on the fact that the UV radiation changes the refractive index locally to produce an additional phase shift [53]. The UV-induced refractive index change required in a 1-mm-long fiber for a $\lambda/4$ phase shift at a wavelength of 1530 nm is $\sim 3.8 \times 10^{-4}$, which is easily achieved. The DFB structure in a rare-earth-doped fiber is useful for ensuring single-frequency operation [9], in much the same way as semiconductor DFB lasers. An inexpensive high-quality fiber-compatible laser exhibiting extremely low noise is particularly attractive for telecommunications. Initial

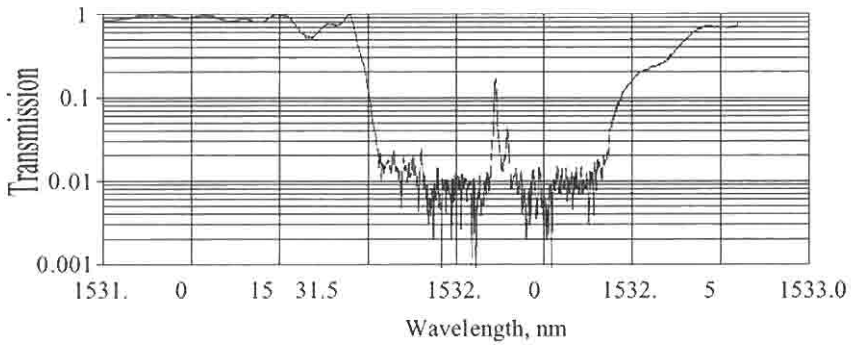

Figure 6.3: Transmission characteristics of an 8-mm-long DFB grating produced by replication of a phase mask with a $\lambda/4$ phase shift in the center [6].

laser diode pumped fiber DFB devices producing ~1 mW single-frequency radiation have already shown the promise of low noise of −160 dB/√Hz [9] (see Chapter 8).

Apodization of the grating leads not only to a smoothing of the side mode structure but also to a reduction in effective length of the grating. The reflectivity is reduced and the band-pass bandwidth increases. There are several apodization envelopes to choose from (see Chapter 5), and they all have a similar effect in unchirped DFB gratings: a reduced reflectivity due to the reduction in the effective length of the grating. Figure 6.4 shows the effect of two such apodization envelopes: the cosine and raised cosine (exponent = 2) for a 3-mm-long DFB with a refractive index modulation amplitude of 1×10^{-3} for both gratings.

Compared to Fig. 6.2, the side-mode structure has been smoothed out. This effect is especially useful for concatenated fiber DFB lasers operating at different wavelengths [10].

The shape of the band pass is not ideal for many applications; a flat top is desirable. In order to increase the bandwidth of the band pass, several concatenated phase steps may be used within a single grating. The principle has been known in filter design [11], and its use was proposed

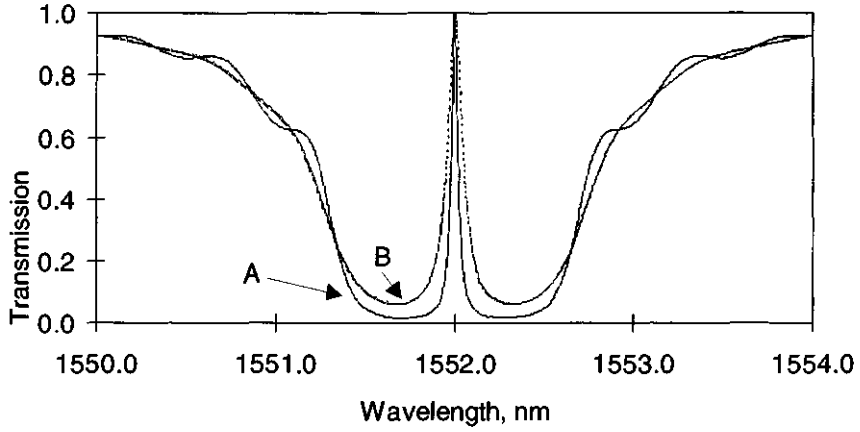

Figure 6.4: Transmission spectra for two 3-mm-long DFB gratings with cosine (A) and raised cosine (B) apodization. The stronger apodization (B) reduces the effective length of the grating and therefore the reflectivity. The FWHM bandwidths of the transmission peaks are 0.1 nm (B) and 0.05 nm (A).

by Haus for semiconductor DFB structures [3,4]. Figure 6.5 shows the practical implementation of such a grating.

Agrawal and Radic [5] have shown that two phase steps place in the grating open a second band pass. The position and size of the phase step shifts the location of the band pass within the band stop of the grating spectrum. The transmission spectrum for a simple case of two symmetrically placed phase shifts of $\pi/2$ is shown in Fig. 6.6.

Two peaks have appeared in the transmission spectrum. The two band-pass peaks can be made to coalesce or move apart by altering the ratio of the lengths of the grating sections. By choosing several phase

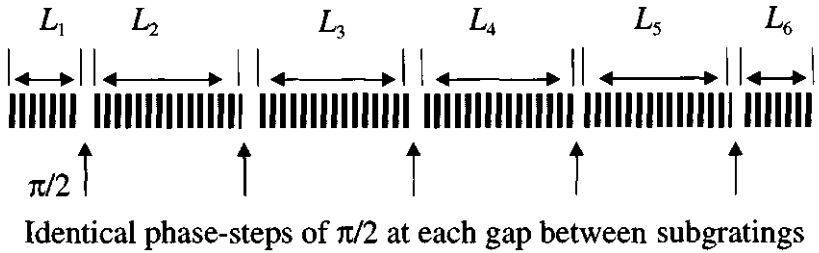

Figure 6.5: The schematic of a cascaded, quarter-wavelength shifted DFB filter, comprising gratings of identical length symmetrically placed around the center.

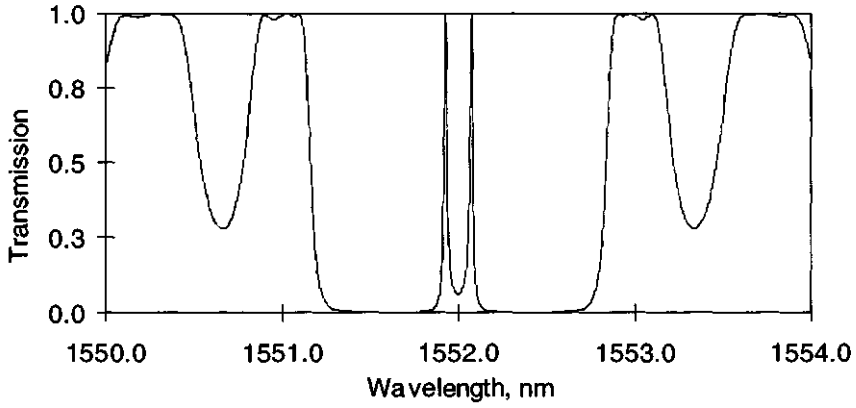

Figure 6.6: A 3-mm-long grating with two $\pi/2$ phase shifts 1 mm apart. The refractive index modulation amplitude is 1×10^{-3}.

shifts Zengerle and Leminger [4] demonstrated the ideal ratios of the lengths of the gratings for an optimized pass band. A quality factor s, defined as the ratio of the pass bandwidth at 10% and 90%, is 0.16 for a single phase-step DFB grating with a coupling constant $\kappa L \approx 2.9$. A length sequence of 1:2:2.17:2.17:2:1 appears to produce a ripple of only 0.3 dB within the pass band with a quality factor of ~0.87. This ratio of the grating lengths will produce the quality factor irrespective of the overall length of the grating. The design was for a semiconductor grating, and the target was for a 0.4-nm band-pass filter. In Fig. 6.5, six gratings are shown with intermediate phase shifts. The lengths $L_1 = L_6 : L_2 = L_5 : L_3 = L_4$ should therefore have the ratio of 1:2:2.17. Note the flat-top pass band.

Wei and Lit [12] have examined symmetrical configurations of 3 and 4 phase-shifted structures. Unity transmission occurs for a symmetrical three-grating-section filter with two $\pi/2$ phase shifts when the grating at either end is half the length of the grating(s) in between. Although this is not a unique condition for unity transmission at the Bragg wavelength (see, for example, Fig. 6.7) in a multisection grating, the three-section and four-section gratings (two phase shifts and three phase shifts) have been shown to have a near unity transmission at the Bragg wavelength if the ratio C of ~2 is maintained; i.e., for the four-section grating, $L_1 : L_2 : L_3 : L_4 \approx 1:2:2:1$, for a variety of coupling constants, κL up to ~2.5. It

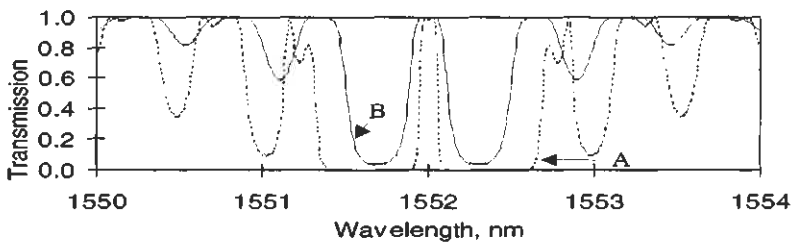

Figure 6.7: Transmission spectrum of two gratings with $4 \times \lambda/4$ cascaded phase step and cosine apodized envelope. Five equal-length gratings of 1.50 mm each have been used, giving a total length ~7.5 mm. The refractive index modulation amplitude is 5×10^{-4}(B) and 1×10^{-3}(A). The FWHM bandwidth of the central pass band is approximately 0.25 nm (B) and 0.1 nm (A); compare with the grating spectra in Fig. 6.4, which have the same individual grating lengths. The bandwidth of (A) above is the same as in Fig. 6.4B, but has a flat top and a squarer profile, with a quality factor of 0.65 (see text) for a κL of ~4.

appears that the ratio for the sections $C = 2$ is an asymptotic value for a flat-top band-pass filter. Increasing this ratio introduces a ripple in the band pass as a result of the individual band-pass peaks separating, while reducing it narrows the bandwidth of the pass band, also reducing the transmission. The ripple in the pass band may be kept between 1% and 5% for a ratio of $1.8 < C < 2.6$.

The bandwidth of the band pass is inversely dependent on the coupling constant. In order to maintain a reasonable bandwidth of the filter, coupling constants must remain low ($\kappa L \sim 1$), as should the grating section ($L_1 < 1$ mm). For example, in the three-section grating, section lengths of 0.5 and 1 mm with a $\kappa L_1 = 1.4$ will result in a bandwidth of ~0.25 nm.

These results change with larger number of sections. For example, Fig. 6.7A shows the transmission spectrum for a grating with a $\kappa L_1 \sim 1.4$, but with a FWHM bandwidth of ~0.1 nm. The bandwidth is exactly the same as the single-phase-step DFB grating shown in Fig. 6.4B, but the square top shows that the roll-off is steeper for the larger number of sections [12]. A major concern is the trade-off between the bandwidth and extinction. For many filter applications, an extinction of >30 dB is necessary. This requirement immediately points to a $\kappa L > 4.16$. Therefore, this filter may not be an ideal candidate, since both requirements may be difficult to achieve.

Fiber Bragg gratings with multiple phase-shifted sections have been realized for band-pass applications. Bhakti and Sansonetti [13] have modeled the response of gratings with up to eight phase-shifted sections. The design strategy was for an optimized band-pass filter with a ~0.8-nm bandwidth, as well as negligible in-band ripple. Increasing the number of sections was shown to make the pass band more rectangular, but reduced the stopped bandwidth. An asymptotic value for the band-stop bandwidth is approached with greater than 5 phase shifts and is twice the pass bandwidth. This is another severe limitation on the use of such filters. Phase masks with the appropriate quarter-wavelength shifts [6] were used to replicate a three-phase-shift grating. With careful UV illumination, the band pass was fully resolved and showed excellent agreement with theory [13]. The band-pass/stop widths were 0.88 nm/2.77 nm with a peak rejection of 13 dB. The optimized grating length were $L_1 = L_4 = 0.22$ mm and $L_2 = L_3 = 0.502$ mm, with a refractive index modulation amplitude of 1.5×10^{-3}.

While the principle of multiple phase shift within a single grating is useful, it has the additional effect of increasing the side-lobe structure despite apodization. The side lobes increase as a result of the formation of a super structure (see Chapter 3) and is discussed in the next section. Other methods need to be used to position the band pass and for a broader-bandwidth band pass and more controllable bandwidth of the band stop.

A simple technique to accurately create a band pass at a particular wavelength is to introduce a phase step within a chirped grating. A start and a stop Bragg wavelength characterize a chirped grating. In a linearly chirped grating, the position of the local Bragg wavelength is uniquely known. Placing a $\pi/2$ phase step at that point results in a band pass at the local Bragg wavelength.

Figure 6.8 shows the transmitted spectrum of two 10-mm-long gratings. Data A and B refer to the same spectrum, with B displayed on a 30 times expanded wavelength scale. A shows the effect of a single quarter-wavelength phase step in the center, while C shows the step at one-third the distance from the long-wavelength end of the grating. The effect of the stitch is localized in the reflected spectrum, and several more band-pass structures may be placed within this grating. For example, a band-pass every 2 nm is easily achieved. However, the effects of the super

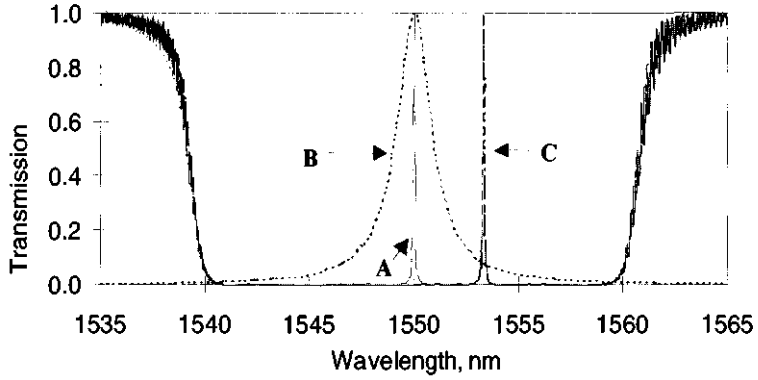

Figure 6.8: The transmission spectrum of a grating with a single $\pi/2$ phase step in the center of a chirped bandwidth of 20 nm (A). An ×30 expanded view of the band-pass spectrum is also shown (B). Also shown is the effect of placing the phase step at $2/3L_g$ (C); the band-pass peak shifts to the local Bragg wavelength. The grating is 10 mm long.

structure become apparent in that additional peaks appear and the band-pass spectrum acquires side lobes. A 10-mm-long grating transmission spectrum with 20 phase steps is shown in Fig. 6.9. Note that within the pass band of the grating there is a small associated dispersion since the grating is chirped. Since the gratings are used as a band-pass, rather than in reflection, dispersion is less of an issue, other than at the band edges. Apodization only helps slightly; it also reduces the bandwidth and the extinction at the edges of the grating, so that it is of limited value.

Blanking-off part of a chirped grating during fabrication instead of introducing phase steps is an effective way of creating a band-pass filter [14]. The net result is that part of the chirped grating is not replicated, thus opening a band gap. This principle is effective for a narrow-bandwidth band pass (1 nm) so long as $\kappa L < \pi$. With a stronger reflectivity grating, the bandwidth of the band stop increases to encroach on the band pass from both sides, reducing the pass-band width. An alternative technique uses UV postprocessing first reported for UV trimming of the refractive index of photosensitive waveguides [53], to erase part of the chirped grating written in a fiber [15]. In order to fabricate a single band pass within a broad stop band (>50 nm), several chirped gratings may be concatenated along side a chirped grating with the band gap. With care and choice of chirped gratings, single and multiple band-pass filters

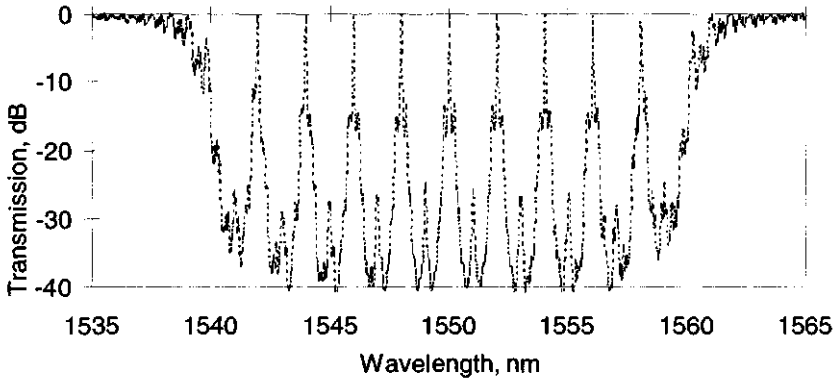

Figure 6.9: A $20 \times \pi/2$ phase-step grating band-pass filter. Each band pass has an extinction of >30 dB, but with some side-lobe structure at −15 dB. Ghosts appear between the main pass bands as a result of the super structure of phase steps at −30 dB transmission.

have been successfully demonstrated, with a pass/stop-bandwidth of 0.17 nm/11.3 nm and extinction of ~10 dB. A four-channel filter evenly spaced over a stop bandwidth of 50 nm has also been reported [15]. Insertion loss of these types of chirped filters is a problem, since radiation loss on the blue-wavelength side affects the maximum transmission of the pass band. As a consequence of large κL and radiation loss, a maximum transmission of ~75% was reported for these band-pass filters.

Broader pass-bandwidth filters may be fabricated by the use of concatenated chirped gratings [16]. The effects of "in-filling" due to the use of large κL values are diminished by increasing the band-pass width. The arrangement for such a filter allows better extinction in the stop band (>30 dB) while permitting the placement of the band-pass at the required wavelength. Additionally, chirped gratings show reasonably smooth stop band edges. Concatenating two such gratings with a nonoverlapping band stop results in a band pass between the two band-stop regions. While this scheme has been applied to chirped gratings, Mizrahi *et al.* [17] have shown that two concatenated highly reflective gratings with a pass band in between the Bragg wavelengths can be used as a band-pass filter. Radiation loss within the pass band are avoided by using a strongly guiding fiber, which further blue-shifts the radiation loss spectrum from the long-wavelength stop band. The bandwidth of the pass band was ~1.6 nm with an extinction in excess of 50 dB and a stop band of ~6 nm.

6.1.2 Superstructure band-pass filter

It has been shown that placing more than a single $\lambda/4$ phase step within the grating results in as many band-pass peaks appearing within the band stop [12]. This principle may be extended to produce the superstructure grating [18,22], but works in reflection. The reflection spectrum has several narrow-bandwidth reflection peaks. The principle has been used in semiconductor lasers to allow step tuning of lasers. However, a badly stitched phase mask will produce similar results. Since a phase mask is generally manufactured by stitching small grating fields together, errors arise if the fields are not positioned correctly. These random "phase errors" are like multiple phase shifts within the grating, resulting in multiple reflection peaks, each with bandwidth inversely proportional to the overall length of the grating, and spaced at wavelength intervals inversely pro-

portional to the length of the field size (see Chapter 3). Figure 6.10 shows the super structure on a 30-mm-long grating reproduced from a phase mask with stitching errors. Despite these errors, the grating reflection and phase response for the main peak are very close to being theoretically perfect [19]. The theory of superstructure gratings is discussed in Chapter 3.

For filter applications, it is necessary to achieve the appropriate characteristics. Here we consider the spectra of short superstructure gratings, which may be conveniently fabricated with an appropriate phase mask. Figure 6.11 shows the reflection and transmission characteristics of a superstructure grating, comprising 11 × 0.182 mm long gratings, each separated by 1.555 mm. The overall envelope of the transmission spectrum (see Fig. 6.11b) has been shown in Chapter 3 to be governed by the bandwidth of the subgrating.

Note in Fig. 6.11a that the bandwidth of the adjacent peaks becomes smaller. This is a function of the reflectivity at the edges of the grating. In order to use this filter as a band-pass filter, it is necessary to invert its reflection spectrum. This may be done by using a fiber coupler. However, the input signal is split into two at the coupler. One half is reflected from the grating and suffers another 3-dB loss penalty in traversing the

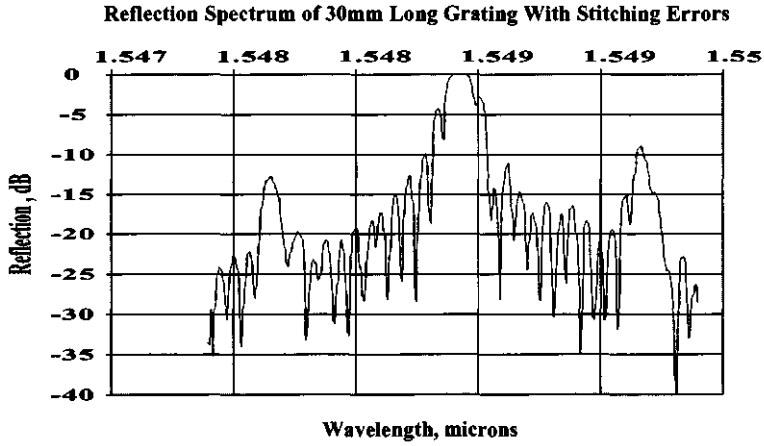

Figure 6.10: Reflection spectrum of superstructure grating. The disadvantage of the superstructure grating—the reflection coefficient cannot be made the same for each reflection [29]. This limitation can be overcome by using a different type of moiré grating [20], which has been discussed in Chapter 3.

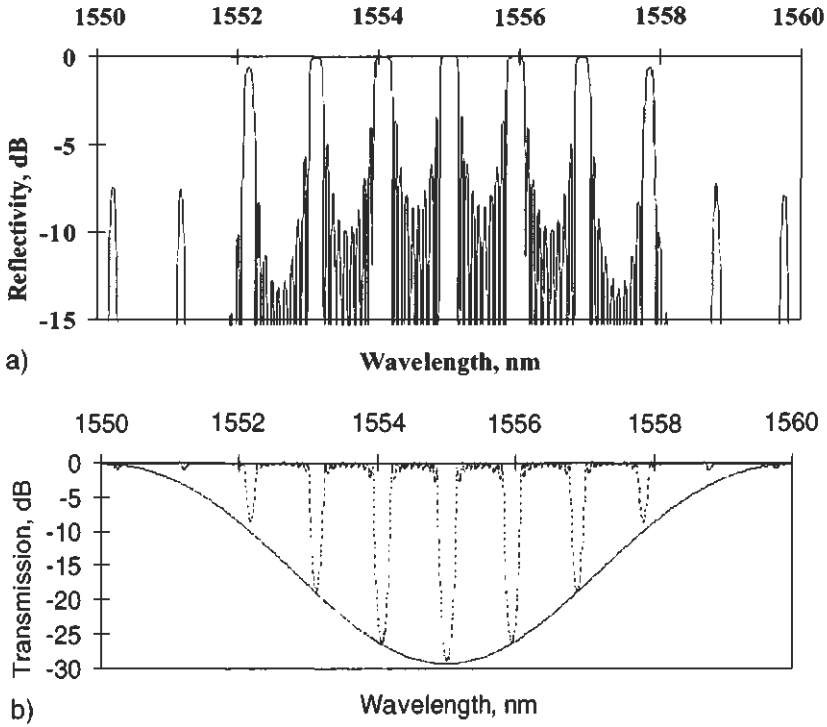

Figure 6.11: (a) The reflectivity spectrum of a superstructure grating with 9×222 micron grating sections separated by 1-mm gaps. Refractive index modulation amplitude is 10^{-3}. (b) The transmission spectrum of the grating shown in (a). Also shown is the transmission spectrum of a single section of the grating of 0.181 microns long. The envelope has been normalized to fit the superstructure spectra.

coupler once again. The reflected spectrum is therefore −6 dB relative to the input signal. A fiber circulator overcomes this loss penalty [21]. The insertion loss of a circulator is approximately 1 dB, so that an efficient multiple band-pass filter can be fabricated.

In an interesting demonstration, a chirped superstructure grating has been used for multiple-channel dispersion compensation, since the repeat band stops have a near-identical chirp [22]. The advantage of such a scheme is that it requires only a single temperature-stabilized grating to equalize several channels simultaneously, although the reflection coefficient varies for each reflection.

6.2 The Fabry–Perot and moiré band-pass filters

The fiber DFB grating is the simplest type of Fabry–Perot (FP) filter. Increasing the gap between the two grating sections enables multiple band-pass peaks to appear within the stop band. The bandwidth and the reflectivity of the gratings determine the free-spectral range and the finesse of the FP filter. The grating FP filter has been theoretically analyzed by Legoubin *et al.* [23]. Equations (6.1.4) and (6.1.5) describe the transfer characteristics of the filter and have been used in the simulation of the gratings in this section.

Figure 6.12 shows the structure of a Fabry–Perot filter. These filters work in the same way as bulk FP interferometers, except that the gratings are narrow-band and are distributed reflectors. A broader bandwidth achieved with chirped gratings creates several band-pass peaks within the stop band. Control of the grating length L and the separation δl allows easy alteration of the stop-band and the free-spectral range.

At zero detuning, the peak reflectivity of a FP filter with identical Bragg gratings is

$$R_{FP} = \frac{4R}{(1 + R)^2}, \tag{6.2.1}$$

where R is the peak reflectivity of each grating. Since the gratings are not point reflectors, the free-spectral range (FSR) is a function of the effective length of the grating, which in turn is dependent on the detuning. For a bulk FP interferometer, e.g., a fiber with mirrors, the FSR is [23]

$$FSR = \frac{1}{2dn_{eff}(\lambda)}. \tag{6.2.2}$$

The distance between the mirrors is d, and the effective index of the mode

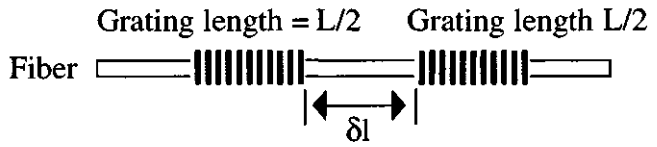

Figure 6.12: A schematic of a Fabry–Perot etalon filter. In the simple configuration, the gratings are identical, although in a more complicated band-pass filter, a dissimilar chirped grating may be used.

n_{eff} is a function of wavelength. For an equivalent fiber-grating-based FP interferometer, the thickness d becomes a function of wavelength, and only at the peak reflectance is the FSR largest. The effective thickness is the separation between the inner edges of the gratings plus twice the effective length of the gratings. Off resonance, the penetration into the grating is greater than on-resonance, leading to a bigger thickness. Therefore, at the edges of the FP bandwidth, the FSR becomes smaller.

The first in-fiber grating FP filter was reported by Huber [24]. A transmission bandwidth of 29 pm was reported. Further multi-band-pass in-fiber FP resonators have also been demonstrated [25]. In the latter report, a 100-mm-long FP interferometer was fabricated with two 95.5% reflecting gratings. A finesse of 67 was achieved with the free spectral range of 1 GHz and a pass bandwidth of 15 MHz. In order to measure the transmission spectrum of the FP, a piezoelectric stretcher was used to scan the fiber etalon in conjunction with a fixed frequency DFB laser source operating within the bandwidth of the grating band stop, at a wavelength of 1299 nm. A peak transmission of ~86% of the fringe maximum was also noted. Figure 6.13 shows the transmission characteristics of a FP filter made with two gratings, each 0.5 mm long with a 5 mm separation and a refractive index modulation of 2×10^{-4}. The weak ripple within the band-stop of the filter is due to the poor finesse of the FP but is ideal in WDM transmission to control solitons. The shortest gratings

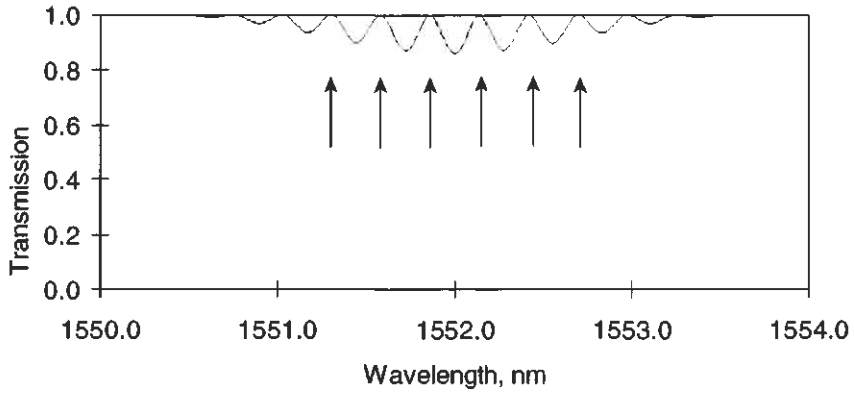

Figure 6.13: A FP filter with a 5-mm gap. Grating lengths are 0.5 mm with index modulation of 2×10^{-4}. The arrows show where WDM channels may be placed within the band-pass filter for soliton guiding.

in a FP filter reported to date are ~0.3 mm long, separated by a similar distance [26]. The resulting multiple band pass, which was a shallow ripple of ~50% transmission was used as a guiding filter in wavelength division multiplexed soliton transmission experiments to suppress Gordon–Haus jitter [27].

With stronger gratings, multiple band-pass filters with deeper band stops are easily possible. However, even slight loss in the grating (absorption due to OH^- ions) can degrade the transmission peaks substantially. It is therefore advantageous to use deuterated fiber for this type of a filter. Figure 6.14 demonstrates a 4-mm-long grating with a gap of 5 mm in the center. This filter shows ~30-dB extinction in the center of the band pass.

Note that all these filters have a similar narrow band-pass response that plagues the highly reflecting DFB grating filter. Thus, applications for such a grating are likely to be in areas in which either high extinction or high finesse, or low extinction and large bandwidth are required. Figure 6.15 shows the measured transmission of a 0.6-mm-long FP filter with a 2.5-mm gap. The pass bands have been measured with a resolution of 0.1 nm and are therefore not fully resolved. The structure should be deeper and much narrower. Nevertheless, the dips in transfer characteristics match the theoretical simulation extremely well with the parameters shown. Typically, the best results for band-pass peaks for this type of FP filter, using either chirped or unchirped gratings with an extinction of 30 dB, is ~70%.

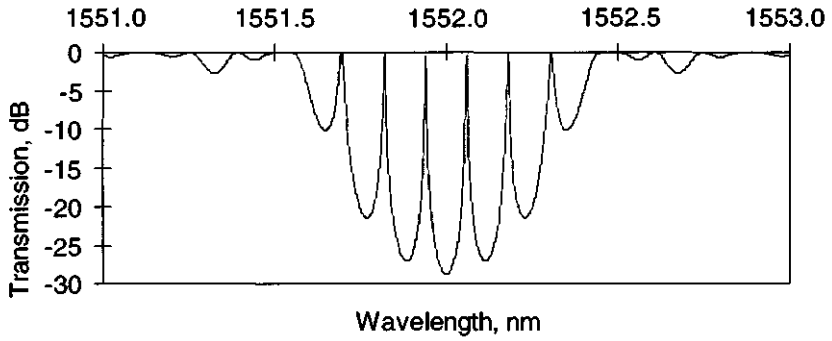

Figure 6.14: A 4-mm-long grating FP filter with a 5-mm gap and a Δn of 5×10^{-4}.

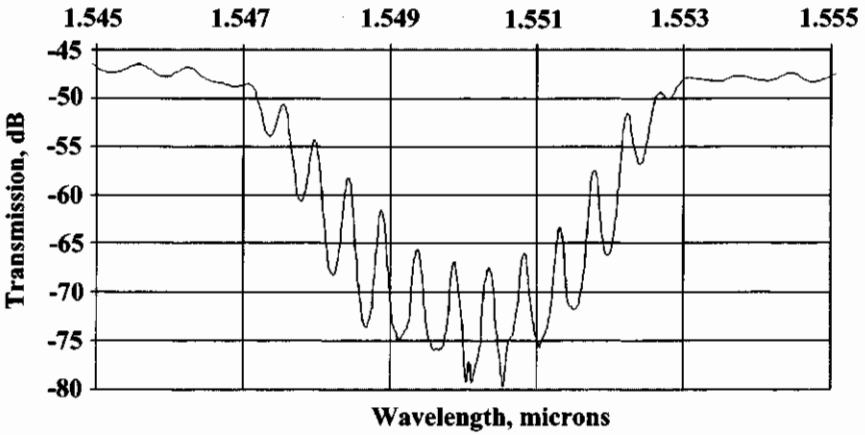

Figure 6.15: Measured transmission characteristics of a fiber FP filter. The length of each grating was 0.3 mm, a 2.5 mm gap and with a peak-to-peak refractive index modulation of 5×10^{-3}. A theoretical fit to the data shows excellent agreement, although the peak transmission has not been fully resolved in the measurement [29]. A maximum extinction of >30 dB was measured.

Wide-bandwidth (140-nm) fiber grating Fabry–Perot filters fabricated in boron–germanium codoped fibers have been demonstrated with a finesse of between 3 and 7 [28]. Two identically chirped, 4-mm-long gratings with a bandwidth of ~150 nm and reflectivity of >50% were written in the fiber, displaced from each other by 8 mm. The resulting FP interference had a bandwidth of 0.03 nm and a free-spectral range of 0.09 nm. A larger free-spectral range was obtained by overlapping the gratings with a linear displacement of 0.5 mm. These gratings had a bandwidth of 175 nm in the 1450–1650 nm wavelength window. A finesse of 1.6 with an FSR of 1.5 nm was demonstrated. These fiber-grating FP-like devices may find applications in fiber laser and WDM transmission systems.

A further possibility of opening up a gap within the stop band is to write two gratings of slightly different Bragg wavelengths at the same location in the fiber [30] to form a moiré fringe pattern. The physical reason why a band pass results may be understood by noticing that the phase responses of the gratings are not identical. Thus, at some wavelength, the phases can be out by π radians. If the wavelength difference is made larger, it is possible to create more than one band pass. The mechanics of producing such a band pass have been demonstrated by

slightly altering the angle of the incoming beams in between the writing of the two gratings [30]. Unless the angle can be measured accurately, it may be difficult to reproduce the results with precision. Two gratings can be superimposed in a fiber by writing one grating with a chirped phase mask [31] and then stretching the fiber before writing the second [32,33]. The basic principle of moiré grating formation is discussed in Chapter 5. However, for clarity, we consider the interference due to two UV intensity patterns to produce a grating with the refractive index profile

$$\Delta n(z) = \Delta n\left[2 + 2\cos\left(\frac{2\pi z}{\Lambda_e}\right)\cos\left(\frac{2\pi z}{\Lambda_g}\right)\right], \tag{6.2.3}$$

in which the slowly varying envelope with period Λ_e is a result of the difference between the two grating periods, and the chirped grating period is Λ_g. If the envelope has a single cosine cycle over the grating length (the grating periods have been chosen to be such; see Chapter 5), then the effect of the zero crossing of the envelope is equivalent to a phase step of $\pi/2$ at the Bragg wavelength (see Chapter 5, Section 5.2.7). This grating is simple to simulate using the matrix method; the apodization profile of the grating can be specified to have n cycles of a cosine function, where $n = 1$ is a single cycle of a cosine envelope (see Fig. 5.18). The computed transmission spectrum of this type of a band-pass filter is shown in Fig. 6.16. The experimentally achieved result is almost identical to that shown in Fig. 6.16 [33], apart from the short-wavelength radiation loss apparent just outside the band-stop spectrum in the measured result.

The problem with this type of phase-shifted grating has already been discussed: There remains a trade-off between bandwidth and extinction, although it is a convenient method of producing a multiple-band-pass filter by increasing the number of cycles of the modulation envelope.

6.3 The Michelson interferometer band-pass filter

The Michelson interferometer (MI) may be used as a fixed-wavelength band-pass filter. Since the coupler shown in Fig. 6.17 splits the input power equally into the two ports, the light that is reflected from a single 100% reflection grating (HR1) is again equally split between ports 1 and 2. Thus, only 25% of the light is available in the pass band at port 2.

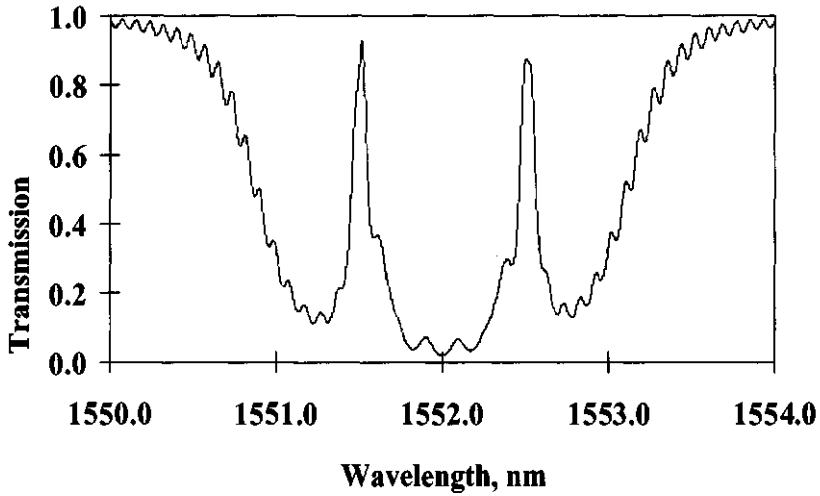

Figure 6.16: Transmission spectrum of a moiré grating with a single period cosine envelope of the modulation refractive index profile over the length of the grating. This grating is formed by colocating two chirped gratings with slightly different center wavelengths.

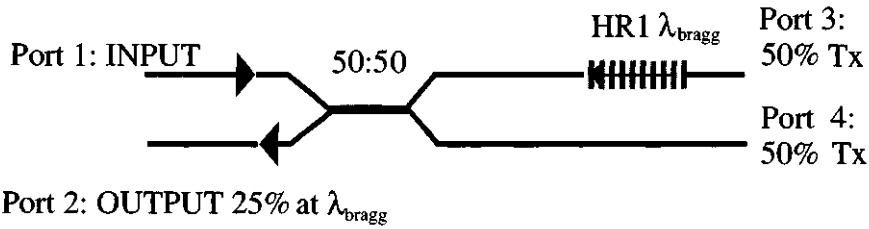

Figure 6.17: A fiber coupler with a single grating in one arm. The output in port 2 is 25% of the input power in port 1. The transmitted signal at the Bragg wavelength at port 3 is $(1 - R)$, where R is the grating reflectivity.

This arrangement works as an effective band-pass filter despite the loss. However, there are methods that be used to eliminate the insertion loss of this filter.

With two identical gratings, one in each arm of the MI, 100% of the reflected light can be routed to port 2. The principle of operation was originally proposed by Hill *et al.* [34], for a grating in a loop mirror

configuration. A similar device is shown in Fig. 6.18. The light reflected from HR2 arrives at the input port π out of phase with respect to light from HR1. Light from HR1 and HR2 arrives in phase at the output port 2, so that 100% of the light at the Bragg wavelength appears at this port. The through light is equally split at ports 3 and 4, incurring a 3-dB loss. However, the phase difference between the reflected wavelengths arriving at the coupler has to be correct for all the light to be routed to port 2.

The first demonstration of such a device in optical fibers was reported by Morey [35]. This all-fiber band-pass filter was made out of a standard fiber coupler with fiber gratings written into the two arms. Stretching the gratings showed limited tunability, but no data was available on stability of the filter. Since differential changes in the ambient temperature between the arms can detune the filter, it is essential that the two arms remain in close proximity and that the optical paths to and from the gratings be minimized.

The fiber Michelson interferometer has been used extensively for sensing applications with broadband mirrors deposited on the ends of the fiber [36]. The principle of operation of the grating-based filter is a simple modification of the equations that describe the broadband mirror device. We begin with the transfer matrix of the fiber coupler [37],

$$\begin{bmatrix} R \\ S \end{bmatrix} = \begin{bmatrix} \cos(\kappa L_c) & -i\sin(\kappa L_c) \\ -i\sin(\kappa L_c) & \cos(\kappa L_c) \end{bmatrix} \begin{bmatrix} A_i \\ B_i \end{bmatrix}, \tag{6.3.1a}$$

where R and S are the output field amplitudes at ports 3 and 4, A_i and B_i are the field amplitudes at ports 1 and 2 of the coupler, L_c is the coupling length of the coupler, and κ is the coupling constant, which

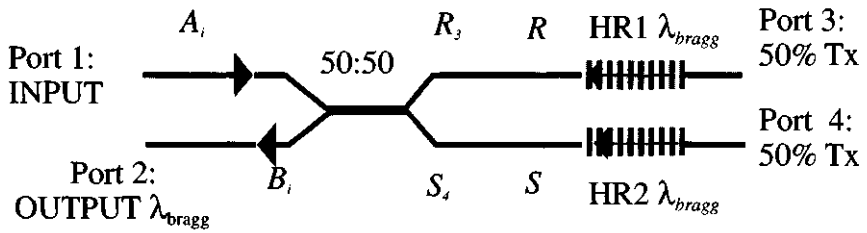

Figure 6.18: The Michelson interferometer band-pass filter. All the input light is equally split at the coupler into the output ports. The identical gratings in each arm reflect light at the Bragg wavelength, while allowing the rest of the radiation through.

depends on the overlap of the electric fields E_1 and E_2 of the coupled modes,

$$\kappa = -\frac{\omega\varepsilon_0}{4P_0}\int_{-\infty}^{+\infty}\int_{-\infty}^{+\infty}(n_{co}^2(x,y) - n_{cl}^2)E_1^* \cdot E_2\, dxdy, \qquad (6.3.1b)$$

where $n_{co}(x, y)$ is the transverse refractive index profile of the waveguides, n_{cl} is the cladding index and, P_0 is the total power.

For a small difference in the propagation constants, $\Delta\beta$ is small compared to the coupling coefficient, κ. Under these conditions, very nearly all the power can be transferred across from one fiber to the other [38]. With $\Delta\beta \approx 0$ and $(n_{co} - n_{cl})/n_{co} \ll 1$, the following expression for the coupling coefficient can be use [39]:

$$\kappa = \frac{\lambda}{2\pi n_c}\frac{u^2}{a^2v^2}\frac{K_0[w(h/a)]}{K_1^2(w)}. \qquad (6.3.1c)$$

a is the core radius, and the normalized waveguide parameters u, v, and w are defined in Chapter 4, h is the distance between the core centers, and the modified Bessel functions of order 0 and 1, K_0 and K_1, are due to the evanescent fields of the modes in the cladding.

Assuming that there is only a single field at the input port 1 of the coupler, $B_i = 0$. Introducing gratings in ports 3 and 4 with amplitude reflectivities and phases, $\rho_1 \exp[i\phi_1(\lambda)]$ and $\rho_2 \exp[i\phi_2(\lambda)]$ described by Eq. (4.3.11), the normalized field amplitudes at the input to the coupler in ports 3 and 4 are

$$\begin{aligned} R_3 &= \frac{A_3}{A_i} = \sigma_1\rho_1 \cos(\kappa L_c)\exp\left[2i\left(\frac{2\pi n_{eff}L_{f1}}{\lambda} + \frac{\phi_1(\lambda)}{2}\right)\right] \\ S_4 &= \frac{B_4}{A_i} = -i\sigma_2\rho_2 \sin(\kappa L_c)\exp\left[2i\left(\frac{2\pi n_{eff}L_{f2}}{\lambda} + \frac{\phi_2(\lambda)}{2}\right)\right], \end{aligned} \qquad (6.3.2)$$

in which the path lengths from the coupler to the gratings are L_{f1} and L_{f2}. The additional factors σ_1 and σ_2 include detrimental effects due to polarization and loss in arms 3 and 4. The output fields, R_1 and S_2, at ports 1 and 2 of the interferometer can be written down by applying Eq. (6.3.1a) again, with the input fields from Eq. (6.3.2). Therefore,

$$\begin{bmatrix} R_1 \\ S_2 \end{bmatrix} = \begin{bmatrix} \cos(\kappa L_c) & -i\sin(\kappa L_c) \\ -i\sin(\kappa L_c) & \cos(\kappa L_c) \end{bmatrix}\begin{bmatrix} R_3 \\ S_4 \end{bmatrix}. \qquad (6.3.3)$$

In Eq. (6.3.3) the normalized field amplitudes R_1 and S_1 fully describe the transmission transfer function of the Michelson interferometer band-

pass filter. Substituting Eq. (6.3.2) into Eq. (6.3.3), and remembering that $\mathrm{Re}(R, S) = 1/2(R, S + R^*, S^*)$, the transmitted power in each output port of the filter is the product of the complex field with their conjugate. By simple expansion and algebraic manipulation of the equations, the power transmittance at ports 1 and 2 can be shown to be

$$t_1 = \frac{1}{2}[2\sigma_1^2\rho_1^2\cos^4(\kappa L_c) + 2\sigma_2^2\rho_2^2\sin^4(\kappa L_c) - \sigma_1\sigma_2\rho_1\rho_2\sin^2(2\kappa L_c)\cos\delta] \quad (6.3.4)$$

$$t_2 = \frac{1}{4}[\sigma_1^2\rho_1^2 + \sigma_2^2\rho_2^2 + 2\sigma_1\sigma_2\rho_1\rho_2\cos\delta]\sin^2(2\kappa L_c), \quad (6.3.5)$$

where the phase difference δ between the reflections from the two gratings is

$$\delta = 2\left[\frac{2\pi n_{eff}}{\lambda}(L_{f_2} - L_{f_1}) + \frac{\phi_2(\lambda) - \phi_1(\lambda)}{2}\right]. \quad (6.3.6)$$

Equations (6.3.4) and (6.3.5) describe how the transmitted power at the output depends on the path-length difference, the reflectivities, and the Bragg wavelengths of the two gratings in the arms of the Michelson interferometer filter. For a 50:50 coupler, $\kappa L_c = \pi/4$; ignoring loss and polarization effects, Eqs. (6.3.5) simplify to

$$t_1 = \frac{1}{2}\left[\frac{1}{2}(\rho_1^2 + \rho_2^2) - \rho_1\rho_2\cos\delta\right] \quad (6.3.7)$$

$$t_2 = \frac{1}{2}\left[\frac{1}{2}(\rho_1^2 + \rho_2^2) + \rho_1\rho_2\cos\delta\right]. \quad (6.3.8)$$

Note that the power transfers is cyclic between the two ports, depending on the phase difference δ and which is of paramount importance for the proper operation of the filter. This cyclic behavior is well known for unbalanced broad band interferometers, but in this device it is restricted to the bandwidth of the gratings. The choice of the gratings determines the wavelength at which the interference will occur. With the phase difference $\delta = 2N\pi$ (where $N \geq 0$ is an integer), all the power is routed to port 1. This phase can to be adjusted mechanically [40], thermally [41], or permanently by optical "trimming" of the path using UV radiation [53].

Detuning of the interferometer is an important issue for the acceptable performance of the band-pass filter. As such, there are two parameters, which are variables in a filter of this type. Assuming that the

bandwidths of the two gratings are identical (nominally identical lengths and refractive index modulation amplitudes), the path difference may drift within the lifetime of the device, or the Bragg wavelengths may not be identical, or may change with time.

Figure 6.19 shows how the band-pass at port 2 varies with changes in the path length for two identical 99.8% reflectivity gratings. At zero phase difference, the transmission is a maximum. The rapid decrease in the band-pass peak with detuning of less than half a wavelength shows that phase stability is critical for the long-term operation of this device. As expected, the transmission drops to zero with a phase difference of $\pi/2$. In most practical cases, it is nearly impossible to match gratings in the two arms exactly, both in reflectivity (and therefore bandwidth) and the Bragg wavelength. The mismatches set a limit to the performance of a band-pass filter.

Figure 6.20 shows the reflectivity spectra of two raised cosine apodized MI gratings, which are offset in their Bragg wavelength by 1% of the FW bandwidth. For the gratings shown, this translates to 0.01 nm difference in the Bragg wavelengths and may well be at the limit of the technology for *routine* inscription and annealing of the gratings.

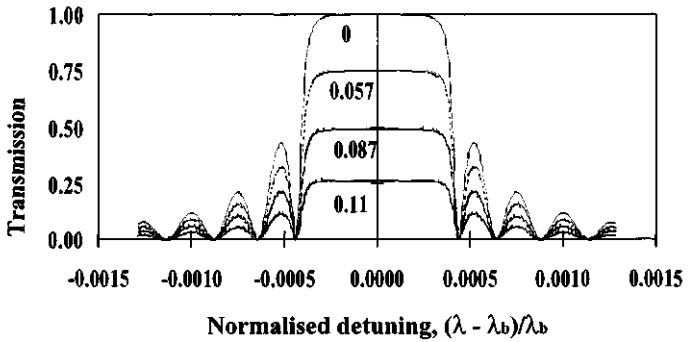

Figure 6.19: The band-pass characteristics of a Michelson interferometer filter showing how the band-pass peak varies with differential path-length difference between the two gratings as a function of normalized detuning. For the calculations, the grating parameters used are: refractive index modulation index amplitude of 1×10^3 and a length of 2 mm [42]. The numbers on the chart refer to the detunings as a fraction of the Bragg wavelength. The figure shows just how critically the path difference needs to be controlled for efficient operation.

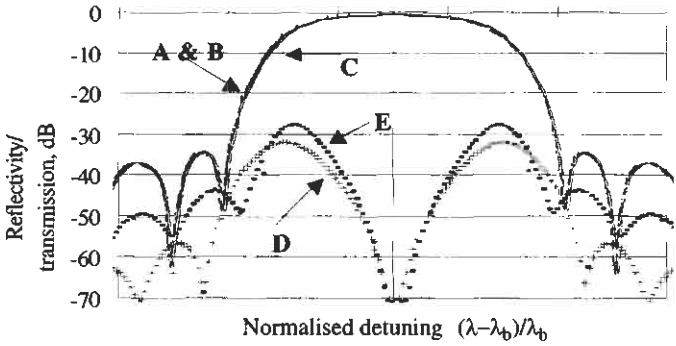

Figure 6.20: Reflection spectra of two 4-mm-long raised cosine apodized gratings mismatched by 0.01 nm (A, B), each with a reflectivity of ~85%. C is the transmission of the band-pass filter with a path-length difference of $0.006 \times \lambda_b$. D shows the light that appears in port 1 of the Michelson. To achieve better than −30 dB extinction (for D), the Bragg wavelengths must be matched to within 0.01 nm. E shows the rejected light in port 1 for cosine apodized gratings with the same Bragg wavelength mismatch. The in-band rejection is never better than −28 dB. With stronger gratings, the Bragg wavelengths have to be even better matched.

The pass band of the filter generally does not suffer from such a small wavelength detuning. Since the reflectivity ensures that only the reflected signal appears in the pass-band with typical insertion losses of between 1 and 0.3 dB [43], it is the remnant signal that appears in the through port (in the Michelson, it is port 1) that is difficult to suppress.

The detuned Bragg wavelength of the gratings translates into an additional imbalance in the path difference of approximately 1 mradian. While UV trimming can balance the paths very accurately, the small difference in the Bragg wavelengths of the two gratings remains. Despite this error, a rejection of greater than 30 dB has been reported [43] and is certainly not an easy achievement, requiring the matching of the Bragg wavelengths to ~0.01 nm. The theoretical spectra shown in Fig. 6.20 are in excellent qualitative agreement with the results of low-insertion-loss band-pass filters fabricated in optical fiber with matched gratings in the close proximity of a coupler [43]. Chirped gratings can be used in the Michelson to broaden the pass bandwidth [44].

With further mismatch in the Bragg wavelengths, the rejection in port 1 deteriorates. One can no longer have a high isolation, since there

is less overlap between the bandwidths of the gratings. The conditions approach the case of a single grating in the coupler arm, when there is no overlap of the grating spectrum. Thus, at least 25% of the input power appears at both ports 1 and 2. While the rejection becomes poor, the band-pass suffers because the bandwidth decreases as a direct result of the limited overlap. Figure 6.21 shows the reflection spectra of gratings in a Michelson that have been detuned by one-quarter of the unapodized FWFZ bandwidth (to the first zeroes). The refractive index modulation amplitude is 1×10^{-3} and the gratings are 4 mm long. Since the interferometer has been detuned as a result of the difference in the Bragg wavelengths, at zero phase difference the band-pass output is not at its maximum (small crosses). As the path difference is changed to $\pi/2$ radians (triangles), a dip begins to appear in the band pass, and with π phase difference (squares), "bat-ears" begin to appear, since at the edges of the band pass,

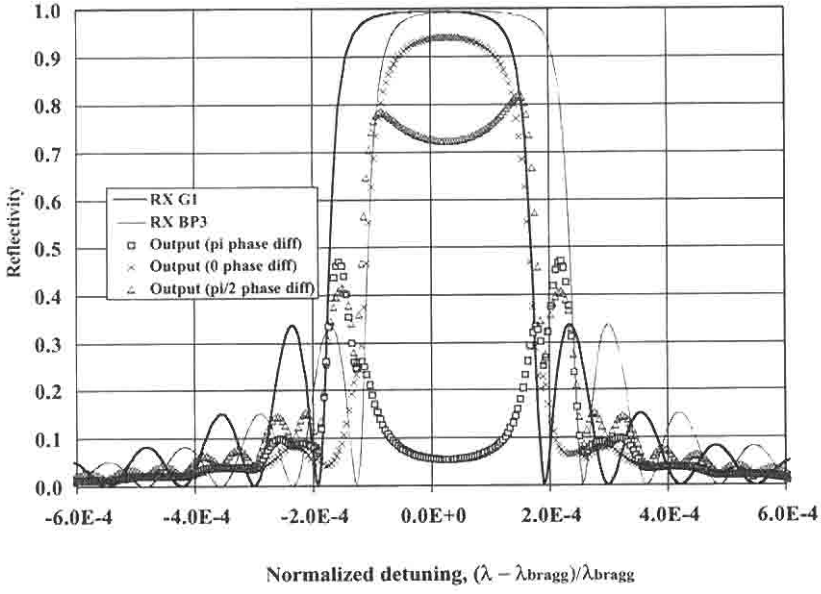

Figure 6.21: The band-pass characteristics show that with slight detuning (0.25 × FW bandwidth) between the two Bragg gratings, a slight reduction in the peak transmissivity occurs (crosses). However, there is an added benefit: reduction in the energy transmitted in the wings of the gratings, i.e., apodization occurs. Note that with larger path length difference, "bat-ears" appear on either side. These normally appear in the rejected port 1 (squares).

there is little overlap of the reflected spectra. Note that at some Bragg wavelength detuning, the interference of the reflected light at the coupler forms moiré fringes, and apodization of the band-pass spectrum begins to occur. In Fig. 6.21 (crosses), note the reduction of the side lobes as the dissimilar phases in the overlapped spectrum tend to cancel the formation of the side lobes.

The filter rejection becomes worse when the detuning is one-half of the FW bandwidth, as shown in Fig. 6.22. In this case, the zero path difference is well off the optimum for band-pass operation (triangles), while squares show the band pass response at π phase difference between the gratings. Although this spectrum is still not the optimized output, note the strong apodization in the wings. The nonoverlapped high-reflectivity (~100%) region (within the bandwidth of each grating) averages to approximately 25% of the input power, as in the case of the single-grating Michelson device.

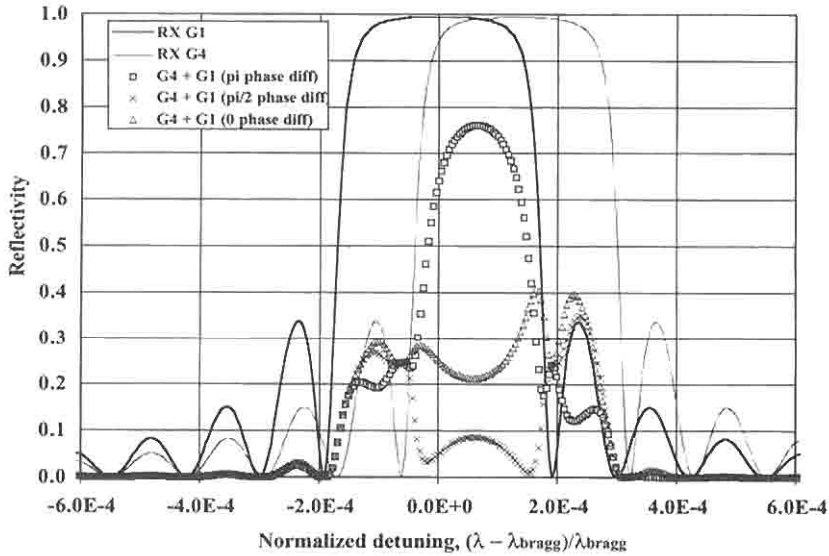

Figure 6.22: Two gratings detuned by approximately 0.5 × bandwidth of the grating. The band-pass characteristics are sensitive to the path-length difference between the Bragg reflection peaks due to differential phase response of the gratings. With detuning, the optimum band-pass shifts from the normal zero phase difference for matched Bragg wavelength case and develops additional structure, although apodization occurs, reducing the reflection in the wings.

6.3.1 The asymmetric Michelson multiple-band-pass filter

Figure 6.19 showed how output power in port 1 varies with path difference δl. The reflected power within the entire grating spectrum is exchanged between port 1 and 2 so long as the detuning

$$\delta l \ll \frac{\lambda^2}{2\Delta\lambda_g}, \tag{6.3.9}$$

where $\Delta\lambda_g$ is the FWFZ bandwidth of the grating. With larger path differences, $n_{\text{eff}}\Delta L_f = n_{\text{eff}}(L_{f1} - L_{f2})$, the phase variation δ as a function of wavelength, according to Eq. (6.3.4), becomes substantial across the bandwidth of the grating. Thus, the single uniform band pass of the filter begins to split into a sinusoidal wavelength with wavelength, restricted to the bandwidth of the grating [42]. Figure 6.23 shows the reflection spectrum of an apodized grating MI and the band-pass output of the filter with a path difference of 0.667 mm. Within the reflection spectrum of the grating, the band pass has three peaks. Each peak automatically has the maximum transmission possible for the band pass, i.e, determined by the reflectivities from the gratings.

With the detuning shown in Fig. 6.24, nine peaks appear within the same bandwidth of approximately ± 0.0005 detuning. Being a nonresonant device, the output is simply equivalent to the interference between

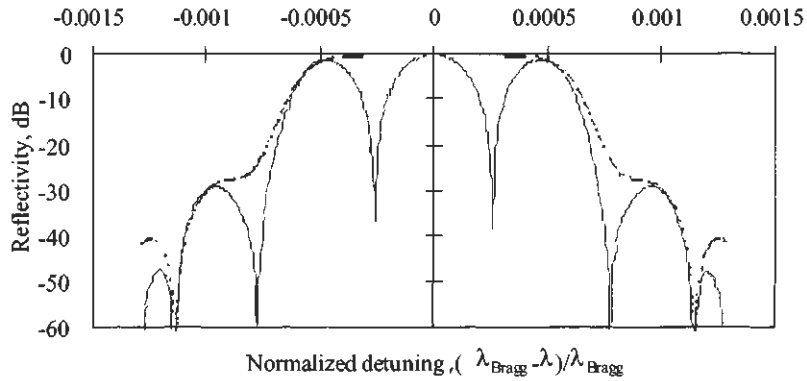

Figure 6.23: The reflectivity and band-pass spectrum of the asymmetric Michelson interferometer. The one-way path imbalance is 0.667 mm and the apodized gratings are 4 mm long with a Δn_{mod} of 1×10^{-3} [42].

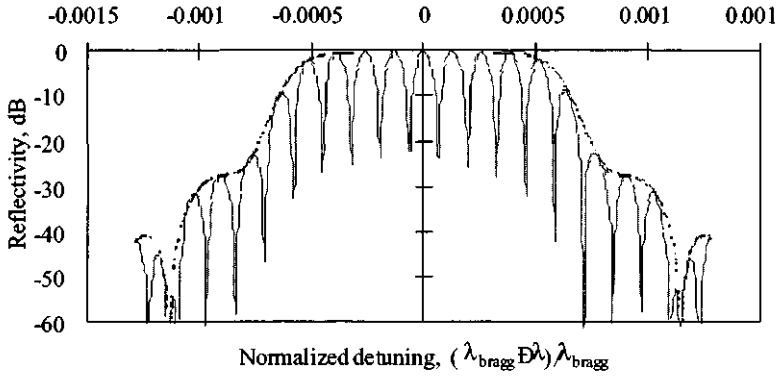

Figure 6.24: The apodized reflection (dashed line) and band pass (continuous line) of the asymmetric Michelson interferometer, with a path difference of 2.67 mm. The output is sinusoidal as in the case of a low-finesse FP interferometer.

two beam as a function of phase difference, hence the sinusoidal variation, also the case with the low-finesse FP interferometer. The wavelength difference $\delta\lambda$ between the peaks of the band pass is

$$\delta\lambda = \frac{\lambda^2}{2n_{eff}\Delta L_f + \Delta\phi(\lambda)}, \tag{6.3.10}$$

where $\Delta\phi(\lambda)$ is the differential phase of the two gratings, which becomes important when the gratings are dissimilar, for example, chirped. Using Eq. (6.3.10) one can calculate the exact number of pass bands within the bandwidth of the gratings. Note that with Bragg-wavelength detuned gratings, the resultant bandwidth for the pass bands is the difference between the individual bandwidths of the gratings. The measured response of such a filter is shown in Fig. 6.25. The extinction is 28 dB.

There are three possible combinations for arranging chirped gratings in the Michelson interferometer: both gratings with the same sign of the chirp, either both positive or both negative, or with opposite chirp. In Fig. 6.26, the first two arrangements are shown (A and B). The difference between A and B is that the dispersion of the gratings has been reversed, and that a pair of such filters may be used to compensate for most of the dispersion in each filter.

The transmission band pass of the identical-sign, linearly chirped grating Michelson interferometer with ΔL_f = 1.724 mm is shown in Fig. 6.27. The gratings are 5 mm long with a chirped bandwidth of 10 nm.

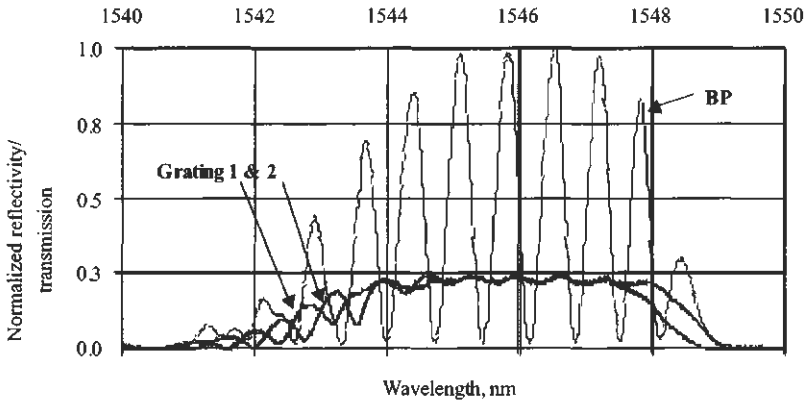

Figure 6.25: The reflection spectrum of each grating (1 and 2) measured *in situ* by bending the fiber in the other port to induce loss: hence the ~25% reflection. The normalized band-pass filter spectrum (BP) as a result of a path difference ΔL_f of ~1.33 mm [42].

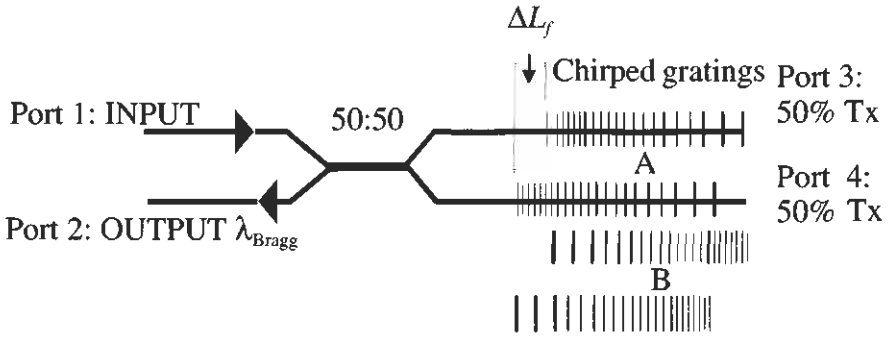

Figure 6.26: Chirped gratings in configurations A and B, each with a path imbalance of ΔL_f but with reversed sign of the chirp.

The unapodized gratings have a Δn_{mod} of 1×10^{-3}. The pass bandwidths of the channels are all identical and equal to the width of the channel spacing. The repeated pass bands can be adjusted by altering the path imbalance; in a demonstration, the paths were adjusted by stretching one arm of the interferometer to fit a grid of 1.1 or 2.2 nm using two 15-nm-bandwidth chirped gratings [45].

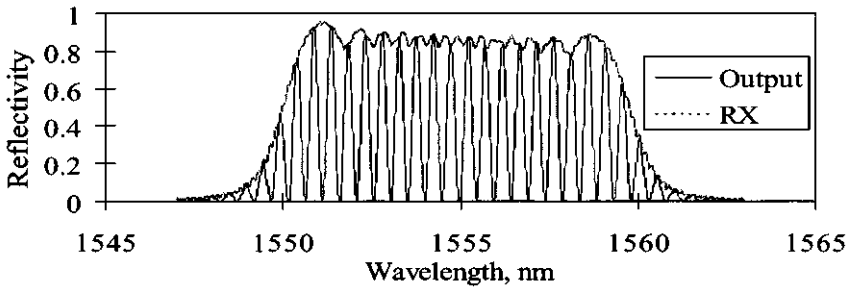

Figure 6.27: Band-pass and reflection spectra with two identically chirped gratings (L_g = 5 mm, chirp = 10 nm, and ΔL_f = 1.724 mm).

When the sign of the chirp of one of the gratings is reversed, the band-pass transmission characteristics change from regular repeated pass bands to a variable pass band. The path difference between the two gratings is reduced to zero at some wavelength. A gap opens at this point and the transmission is no longer uniform as in the previous cases. Ignoring dispersion, the phase difference between the light reflected from these two weakly reflecting, chirped gratings with a chirp of $\Delta\lambda_g$ nm relative to the wavelength λ_0 in the center of the grating, is

$$\begin{aligned}\delta(\lambda) &= \frac{4\pi n_{eff} L_g}{\lambda}\left(\frac{\lambda_0 - \lambda}{\Delta\lambda_g}\right) - \frac{4\pi n_{eff} L_g}{\lambda}\left(\frac{\lambda - \lambda_0}{\Delta\lambda_g}\right) + \frac{4\pi n_{eff}\Delta L_f}{\lambda} \\ &= \frac{4\pi n_{eff} L_g}{\lambda}\left[2\left(\frac{\lambda_0 - \lambda}{\Delta\lambda_g}\right) + \frac{\Delta L_f}{L_g}\right],\end{aligned} \tag{6.3.11}$$

where L_g is the length of the grating. It is apparent from Eq. (6.3.11) that the detuning $\delta = 0$ when

$$\lambda = \lambda_0 - \frac{\Delta\lambda_g \Delta\Delta L_f}{2L_g}. \tag{6.3.12}$$

If $\Delta L_f = 0$, $\delta = 0$ at the wavelength $\lambda = \lambda_0$. For a fixed chirp bandwidth, the detuning can be reduced to zero at any wavelength within the bandwidth of the grating by tuning ΔL_f. In Eq. (6.3.11) we have assumed that the lengths of the two gratings are identical. This need not be the case; it is enough that the bandwidth are identical, so that we have the extra parameter that can be adjusted. This also applies to the previous cases in which the sign of the chirp for both gratings was identical. The pass-

band period is now chirped, since the variation in the detuning is no longer constant close to the phase-matching wavelength.

Figures 6.28 and 6.29 demonstrate the effect of the counter-chirp of the gratings for the more general case of dissimilar length gratings. At the top of Fig. 6.28 is shown a schematic of the third combination for the chirped gratings (C) and the relative positions, orientations and lengths

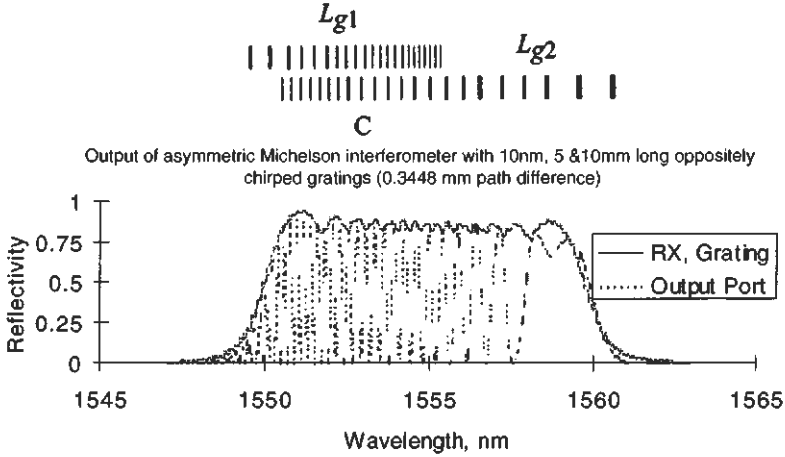

Figure 6.28: Above the chart is shown the arrangement of the gratings (C) used in this simulation of the asymmetrically placed grating Michelson interferometer BP with identical chirp bandwidth but dissimilar lengths (5 and 10 mm). Notice the chirp in the period of the pass bands. The reflectivity of one of the gratings is also shown.

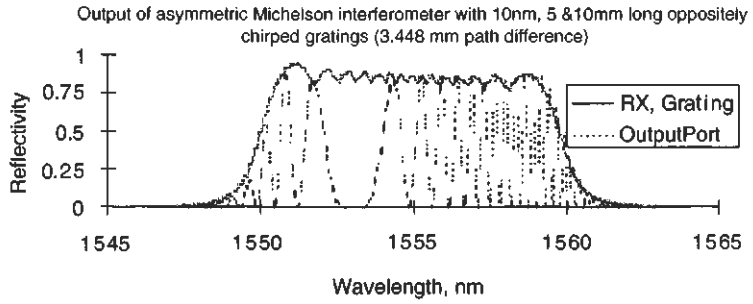

Figure 6.29: The band-pass response with a 3.448-mm path difference.

of the gratings. The first case is for 10- and 5-mm-long gratings, each with a chirped bandwidth of 10 nm and with a detuning of 0.344 mm (Fig. 6.28). The gap opens up close to one long-wavelength end of the grating, while with a larger ΔL_f of 3.44 mm in the second case, the gap shifts to the short wavelength end (Fig. 6.29). In either case, moving away from the phase-matching point [Eq. (6.3.12], the oscillations in the transmission spectrum become more rapid.

There are important issues relating to the asymmetric grating Michelson interferometer band-pass filter. First of all, any interferometer is sensitive to *differential* temperature and strain. The asymmetric interferometer is especially so; however, with fiber leads to the gratings kept in close proximity, the only region, which needs stabilization, is the *differential* path. For sensing applications, the broad bandwidth of the chirped grating is a distinct advantage. Stabilization of the paths may be done in a number of ways, for example by the application of a special polymer coating [46,47], or use of a substrate to compensate for the thermal expansion [48]. The filter has very high extinction, but the stability is polarization sensitive, and the transfer characteristics are sinusoidal with wavelength. The period and chirp are easily designed into the filter. Applications may be found in signal processing, sensors, multiplexing, and spectral slicing within a well-defined bandwidth. Ideally, it would be suited to fabrication in fused fibers, close to the coupler, or in planar form.

6.4 The Mach-Zehnder interferometer band-pass filter

The dual-grating Mach-Zehnder interferometer band-pass filter (GMZI-BPF) overcomes the severe limitation of the Michelson interferometer filter — the loss of 50% of the through transmitted light — by recombining the output at a coupler, as shown in Fig. 6.30. The scheme was proposed by Johnson *et al.* [49], and using etched gratings in a semiconductor waveguide Mach-Zehnder interferometer, Ragdale *et al.* [50] were able to show a device operation. A major drawback of a device fabricated in this way is the high intrinsic losses due to scatter, absorption, and input/output coupling, although large bandwidths are possible due to the use of short gratings resulting from the large modulation index of the grating (air and semiconductor). Additionally, once the device has been fabricated,

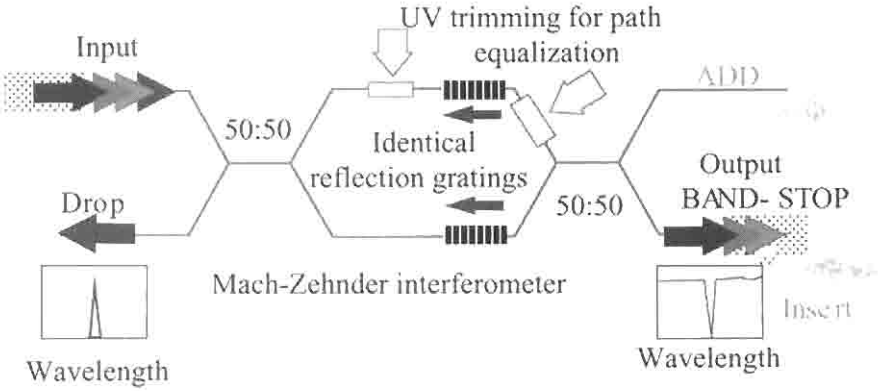

Figure 6.30: The Mach–Zehnder interferometer used as a band-pass filter. UV trimming of the paths has been shown to be a powerful tool for rebalancing the paths such that 100% of the light reflected from the gratings appears at the output port on the left [53,43]. By adjusting the phase difference at the coupler beyond the gratings, the output may be directed to either output port of the coupler.

phase adjustment between the guides to balance the interferometer is difficult without active control.

The first demonstration of a working band-pass device using the principle of the Mach–Zehnder interferometer (MZI) with two identical UV written gratings was in planar-Ge:silica waveguide form [53]. The device was an MZI with overclad ridge waveguides, which had been photosensitized using hot-hydrogen treatment [51]. "UV trimming" was used to balance the interferometer after the gratings were written, demonstrating this powerful technique also for the first time [53]. This is shown Fig. 6.30. "UV trimming" relies on photoinduced change in the refractive index to adjust the optical path-length difference. The 6-dB insertion loss for a single-grating band-pass filter was overcome and reducer to ~1.34 dB for the fiber pigtailed device, by UV trimming; much of it comprised coupling and intrinsic waveguide loss. The fiber gratings had a reflectivity of ~15 dB each and were well matched in wavelength. Approximately 10% of the light was reflected into the input port. Although the insertion loss of this MZI-BPF was not as low as later devices, the planar MZI has the advantage of being extremely stable to environmental effects. Since the demonstration, several groups used this scheme of UV trimming in fiber-based MZIs to demonstrate band-pass filters with better extinction and

insertion loss [43,52]. For proper operation, the output coupler needs to be balanced, requiring trimming on the RHSs of the gratings.

Indeed, it is simple to observe that the device can be used as an add multiplexer at the dropped wavelength if the same wavelength is locally injected at the port marked "Insert" (RHS, bottom). This wavelength will be routed through to the Add port performing the basic Add–Drop multiplexer function. Many of these MZIs may be cascaded to perform a multiple-wavelength band-pass function.

Cullen *et al.* [52] demonstrated a compact GMZI-BPF in fiber form. The device, based on two 50:50 splitting fused fiber couplers fabricated in boron–germania codoped fibers (Core–cladding index difference $\Delta n = 7 \times 10^{-3}$ and core diameter of 7 μm), with 1-meter tails. The two pieces of fiber were first tapered and fused to a constant diameter of 100 μm over a length of 20 mm. A 3-dB coupler was formed by further tapering one end of the fused region, until the desired splitting ratio of 50% was achieved. When the second coupler is made, if the path lengths in the two arms are identical, 100% of the light will appear in the crossed state, i.e., in port 4 when port 1 is excited. Allowing for fabrication loss and slight imbalance, between 95 and 99% of the light was available at port 4 after the second coupler was fabricated under the same conditions. The finished device had ~5 mm of space in the parallel fiber section between the couplers for the inscription of the gratings and for UV trimming. The advantage of such a structure is the relative stability of the MZI, since the couplers and the fused fiber regions are so close together. Any ambient temperature fluctuations affect both fibers equally. This was established by a measured change in the output power of the MZI of <0.05 dB over a temperature excursion of −20 to +60°C, with a wavelength window of 40 nm. It is necessary to mount the fibers on a mechanical support in order to proceed with grating inscription. A silica microscope slide is ideal for this application, since it enables the device to be supported, handled, aligned in the interferometer. For this device, gratings of 3-mm length were written in both arms under identical conditions using an intracavity CW frequency-doubled argon ion laser. The grating reflectivity can be monitored accurately by the size of the dip from the transmitted level at a few nanometers on the long-wavelength side of the Bragg wavelength (to avoid the radiation loss region on the blue side, as well as the side lobes on the red side of the grating spectrum). Once the two gratings are written using identical conditions, the device can be balanced by examining the reflection in port 1. Ideally, either a coupler or a circulator

may be used to monitor the reflection while optical trimming is undertaken in the region closest to port 1, to *minimize* the reflection at the Bragg wavelength [53]. Lastly, the output ports need to be balanced by trimming on the far side of the gratings. The power on the long-wavelength side of the Bragg wavelength can be steered to either port 3 or 4 as necessary. In their device Cullen *et al.* [52] reported an insertion loss of only 0.5 dB, and 0.35 dB for a standard fiber device. With 99% reflectors, strong radiation loss was noted on the blue side of the Bragg wavelength.

The long-term stability of the GMZI-BPF depends on the stability of the substrate and the uniformity of the stress and temperature gradients. Silica for the substrate is a good choice since it is better matched to the properties of the fiber. However, the Bragg wavelength in Ge:doped fiber shifts by ~16 pm/°C. Compensation of the drift can be countered by the use of packaging with an effective negative thermal expansion coefficient [54–56,47,48]. Athermalization using a β-eucrytite glass substrate has been shown to reduce the temperature sensitivity of fiber Bragg gratings to ~0.0022 nm/°C, and the drift in the wavelength was measured to be 0.02 nm after thermal cycling 60 times over a temperature excursion from −40°C to +85°C [56]. The glass is based on a stuffed derivative of the crystalline phase, β-quartz (LiO_2:Al_2O_3:$2SiO_2$). Normally, this phase has a large negative thermal expansion coefficient along the *c*-axis but forms a poor glass. Nucleated with TiO_2 and adjusting the glass composition to form β-eucrytite results in a stable glass melt. Heat treatment at above 1200°C forms the glass ceramic with the appropriate crystalline microstructure for a negative thermal expansion coefficient.

The principle of athermalization of delay through a fiber using a tube of oriented liquid-crystalline polymer [54] has also been used to athermalize gratings. A measured $d\lambda_{Bragg}/dT$ of 0.01 nm/°C for the uncompensated FBG was reduced to 0.13 nm/100°C after compensation, with no significant hysteresis during the temperature cycling from −40 to +80 °C [47]. Use of such materials as substrates for the GMZI-BP should result in robust devices.

6.4.1 Optical add–drop multiplexers based on the GMZI-BPF

Changing the phase in one of the arms of the MZI between the coupler and the gratings routes the reflected light to either the "drop" or the "input" port. Any method that can reliably alter the phase can be used

to switch the OADM. The parameters that can be altered are temperature [40,41] or strain to alter the phase difference between the arms of the MZI, or the Bragg wavelength of the gratings. To alter output state, the phase in one arm can be tuned reliably and requires a 10-mm length of fiber to be heated by~13°C. With strain, a fiber extension of $1/4\lambda_{\text{Bragg}}$ is required to switch the OADM.

Temperature tuning of the gratings requires a 65°C change to shift the fiber Bragg grating wavelength by ~0.8 nm. If the channels are spaced 1.6 nm apart, then a channel may be dropped by tuning the Bragg wavelength to match the channel wavelength and deselected by detuning. Tuning both gratings simultaneously by either strain or temperature while maintaining interferometric stability is not easy, so, this device requires careful engineering.

The GMZI-BPF can be used as an optical add–drop multiplexer (OADM). If the phase in one of the arms can be controlled actively, e.g., by a piezoelectric stretcher, then a wavelength may be either switched to the drop port or reflected back to the source. The insert function is operated in a similar manner by the use of a second piezoelectric stretcher on the RHS of one of the gratings in the MZI. The "drop" and "add" ports have fiber-coupler taps to monitor the state of the output and to control the piezoelectric stretchers to switch the GMZI-BPF using phase-locked loops [40]. A disadvantage of this scheme is that it always blocks the transmission of the channel, whether it is dropped or not, and it must be reinserted for forward transmission.

Mizuochi and Kitayama [57] combined a set of GMZI-BPFs to perform a two wavelength OADM function, which is shown in Fig. 6.31. The basic element of the device is a double GMZI-BPF with four identical gratings in the two MZIs, as well as an additional highly reflecting grating as an "isolator" between the two MZIs, shown in the top half of Fig. 6.31. The function of the additional grating is to prevent light at the grating Bragg wavelength from crossing from one MZI to the other, increasing isolation. This is particularly important because light inserted into the OADM can cross from one MZI to the other (from left to right and the reverse) to cause in-band coherent beat noise [58] (see Section 6.5). Light arriving from the left in the top half at port A1 is dropped at the Bragg wavelength λ_i and routed to the second GMZI-BPF in the lower half of the figure, containing gratings at another wavelength, λ_j. The dropped wavelength, λ_i therefore appears at C1. Similarly, light injected in C2 at the wavelength λ_i uses the "add" part of the top GMZI-BPF on the

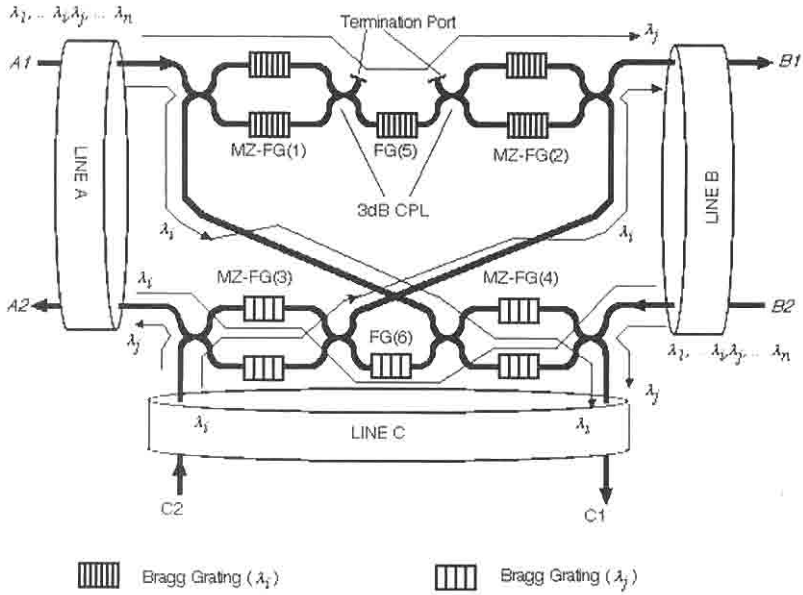

Figure 6.31: A two-wavelength cascaded GMZI-BPF with increased isolation between the add and drop ports (from: Mizuochi T. and Kitayama T., "Interferometric cross talk-free optical add/drop multiplexer using cascaded Mach-Zehnder fiber gratings," in *Technical Proc. of OFC '97*, pp. 176–177, 1997.) [57].

RHS and is routed to B2. All other wavelengths arriving at A1 simply go through the gratings and also appear at B1. Similarly, channels arriving at B2 are routed to A2, except for the channel at λ_j, which is dropped at C1 and reinserted from C2, to be routed to A2. The inclusion of the "isolating" grating reduces the leakage between A1 and B1 from -26 to -71 dB. The improvement is evident in the add–drop function, by a reduction in the power penalty of 1 dB due to the elimination of coherent beat noise. The use of higher reflectivity gratings in the MZIs should eliminate the need for the "isolator" grating, although short-wavelength radiation loss will remain a problem.

6.5 The optical circulator based OADM

The optical circulator has become extremely important for applications with fiber gratings. While the use of a fiber grating with a circulator is

an obvious method for converting the band stop to a band-pass filter, it is worthwhile to consider the benefits of such a configuration. The first reported use was as an ASE filter for an erbium amplifier [59]. The amplified signal is routed to the input of a circulator and reflected by a narrow-bandwidth grating in the second port. The grating filters the amplified spontaneous emission from the amplifier and routes the signal to the output port. The reduction in the out-of-band spontaneous emission can be considerable, but is determined by the quality of the reflectivity spectrum of the grating. Optical circulators have an insertion loss of only ~1 dB, turning this very simple device into a superb band-pass filter. Several gratings with different Bragg wavelengths may be cascaded to form a multiple band-pass filter. The addition of a second circulator leads to a simple method of performing an optical circulator based add–drop multiplexing (OC-ADM) function using gratings and is shown in Fig. 6.32. Channels injected at the "input" port are reflected by the gratings in between the two circulators and routed to the "drop" port. All other wavelengths continue to the "output" port. If the signals are injected at the "insert" port on the RHS of Fig. 6.32, the same gratings perform an insert function, routing the reflected channels to the "output" port, along with the rest of the channels from the "input" port. The low polarization sensi-

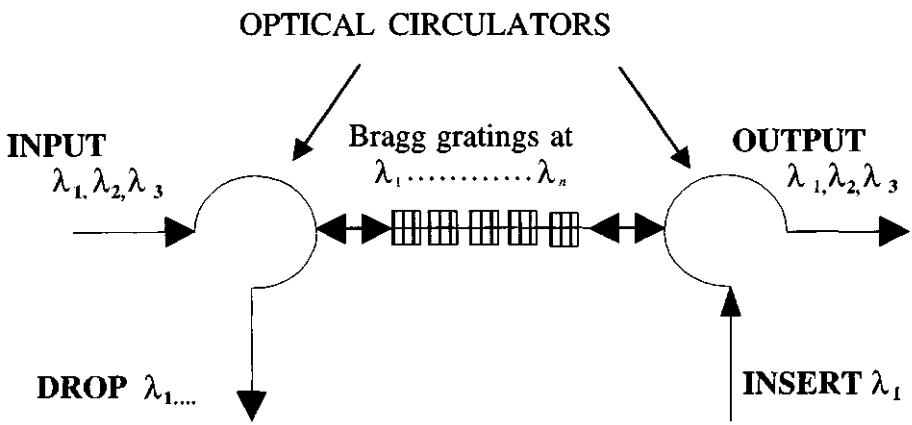

Figure 6.32: An OC-ADM using an all optical circulator. This device allows several channels to be dropped or added according to the number of fiber gratings between the circulators. The signal at the Bragg wavelengths are reflected and appear at the drop port, while the same gratings may be used to insert the same channels for wavelength reuse from the insert port.

tivity and extremely high return loss of the circulators are a distinct advantage for this type of function, despite their insertion loss of ~1 dB. Since the circulator-fiber grating band-pass filter is not interferometric, it is intrinsically stable in its operation, but remains an expensive solution for some application. However, for amplified long-haul fiber communication routes with large capacity (e.g., submarine systems), the cost of a few of circulators is unlikely to be an overriding factor.

The issues that need to be addressed with the OC-ADM are the channel-dependent insertion loss, intra- and cross-channel cross-talk, and the dispersion penalty due to the bandwidth of the gratings. Channel-dependent loss is primarily due to the "blue-wavelength" radiation loss exhibited by all fiber Bragg gratings. Thus, reflected light from the shorter-wavelength gratings may experience loss either in the drop *or* in the add function, unless the gratings are fabricated with care. Figure 6.32 shows a sequence of gratings reflecting at λ_1, $\lambda_2 \ldots \lambda_n$. The gratings are arranged so that the first grating reflects at the shortest wavelength and the last, λ_n, at the longest. A highly reflective grating transmission spectrum is shown in Fig. 6.33. The loss on the blue-wavelength side extends over a wide bandwidth. If each grating has similar transmission characteristics, spaced, say, 10 nm apart, the blue-wavelength radiation loss will increase with each additional grating. Light injected from the short wavelength side (e.g., from the "input" port) is reflected in sequence, so that the shortest wavelength is reflected first, and then the second shortest, and so on. Each wavelength λ_n has to traverse $n - 1$ gratings

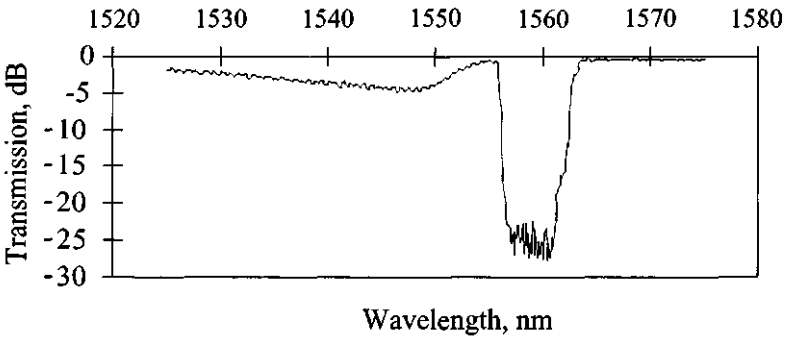

Figure 6.33: The measured transmission spectrum of a 7-nm full-bandwidth, highly reflecting chirped grating with the associated "blue"-wavelength loss extending over almost the entire gain bandwidth of an erbium amplifier.

reflecting at a wavelength *shorter* than λ_n. However, since the loss in traversing the grating is always on the short-wavelength side of the Bragg wavelength, each wavelength is reflected *without* incurring radiation loss.

The situation is different if the order of reflection is reversed, as is the case when the light is injected into the "insert" port. The longest wavelength is reflected first and so does not incur loss. The next wavelength (in this example, at ~1550 nm) to be reflected lies on the short-wavelength side of the reflection shown Fig. 6.32 and so suffers twice the radiation loss α of approximately 6–8 dB. Again, each wavelength λ_n has to traverse $n - 1$ gratings reflecting at *longer* wavelengths and suffers a loss of $(n - 1) \times \alpha$ dB. This loss causes severe skew in the wavelength response of the OADM. Although the radiation loss spectrum shown in Fig. 6.33 is very high and has a large bandwidth, the insertion loss argument applies to all such OADM devices. The insertion loss varies across the bandwidth but is always cumulative in one direction and can be more important for wavelengths that have not been dropped but lie on the short-wavelength side of the OADM. There are methods that can be used to reduce the radiation loss of the gratings, for example, by design of the fiber [60,61] to suppress radiation mode coupling, or by choosing the channel spacing such that none lie in the radiation loss region [17].

Intrachannel cross-talk occurs if the added channel is derived from the same source as the dropped channel and leaks through from the "insert" to the "drop" port. If a strong signal is added at the OADM, a small fraction leaks through to the drop port if the grating reflectivity is not very high. This small "breakthrough" can be of the same order of magnitude as the signal, which has been attenuated by the link loss and dropped at the OADM. If the added and dropped wavelengths are the same, signal beat noise occurs and degrades the bit error rate (BER). Alternatively, the breakthrough signal can cause simple cross-talk between adjacent channels that are dropped, in the same way it can be transmitted to the "add" port. The associated power penalty has been calculated to be

$$p_{coherent} = -10 \log(1 - 4\sqrt{r}) \tag{6.5.1}$$

for a ratio r of the leaked "add" and the dropped signal powers for coherent signals. This is much higher than for incoherent signals [62], for which

$$p_{incoherent} = -10 \log(1 - r). \tag{6.5.2}$$

Dispersion due to the gratings is an issue, which depends on the signal and grating bandwidths. Gratings show strong dispersion at the

edges of the reflection band (see Chapter 4). If the signal fills the grating or is severely limited by the grating bandwidth, apart from the simple pulse broadening (narrowed spectrum), additional dispersion from the band edges of the grating has the potential of causing severe pulse distortion. This area has only recently received attention [63].

Programmability of an OADM is often desirable, and there are several techniques available to integrate this feature. As has been seen with the GMZI-BPF, the most easily adjustable parameter is the path length difference from the coupler to the gratings, since tuning the Bragg wavelength of both gratings poses a difficult engineering problem. The OC-ADM is not an interferometric device, so that tuning of the gratings by stretching/compressing or heating is easily achieved. Quetel *et al.* [65] demonstrated this principle with a circulator and four gratings stretch tuned by piezoelectric (PZT) actuators, with a switching time of 40 μs and a voltage of only 50 V. Okayama *et al.* [64] proposed the use of a pair of identical gratings for each add/drop channel with two 4-port optical circulators for an OC-based tunable add–drop multiplexer (OC-TADM). Figure 6.34 shows the arrangement of the gratings for a four-channel OC-TADM. Channels arriving at the input port are reflected by the appropriate gratings, λ_1, λ_2, λ_4 in the top part of the circulator branch, *group* 1. Gratings 2 and 4 are tunable (by either temperature or strain); however, all channels are reflected and routed to the second set of gratings, λ_4, λ_2, λ_2, λ_1 in the bottom part of the circulator branch, *group* 2. In this section, gratings 3 and 1 are tunable. If each grating pair has identical Bragg wavelengths, *all* channels are routed to the drop port by reflections from *group* 2 gratings. However, since one of the gratings of the matched pair

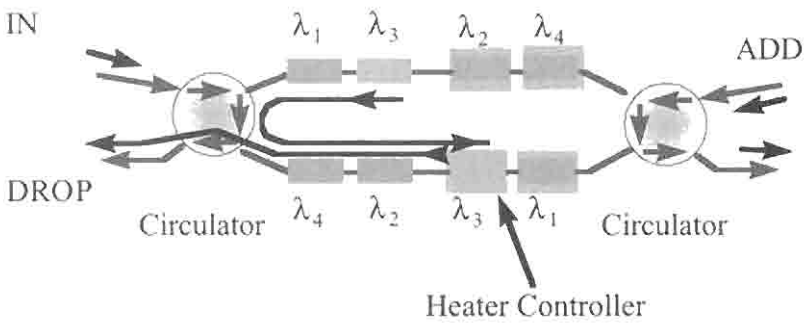

Figure 6.34: Dynamic wavelength selective add/drop mux–demux using tunable gratings (after Ref. [64]).

is tunable, it can be detuned, thus directing the channel at that wavelength to the through port.

Since the device is symmetric, the channel insert function is performed in a similar manner: When injected into the "add" port, the wavelengths are routed to the "through" port. Poor peak and high side-lobe reflectivity cause cross-talk. The use of unapodized (−14 dB side-lobes), 95% peak reflectivity gratings resulted with in poor cross-talk performance. With well-apodized, high-reflectivity gratings, low cross-talk performance is possible and the OC-TADM is appropriate for dense-WDM applications. In principle, piezoelectric stretchers can be used to make a fast OC-TADM, switchable in < 1 μs [65].

In a slightly simpler arrangement, Kim *et al.* [66] proposed the use of four identical gratings between two three-port circulators. The gratings are stretch tuned by piezoelectric stretchers, so that up to four channels can be dropped or inserted in any combination, when the Bragg wavelengths of the gratings are tuned to the channel wavelengths. Mechanical leverage designed into the grating mounts with the piezoelectric stretcher allows the Bragg wavelength of each grating to be tuned by 2.4 nm/120 V applied.

6.5.1 Reconfigurable OADM

These devices are based on optical switches and circulators and overcome some of the limitations of the OC-TADM and the GMZI-BPF. A schematic of the reconfigurable OADM (ROADM) is shown in Fig. 6.35. Two fiber

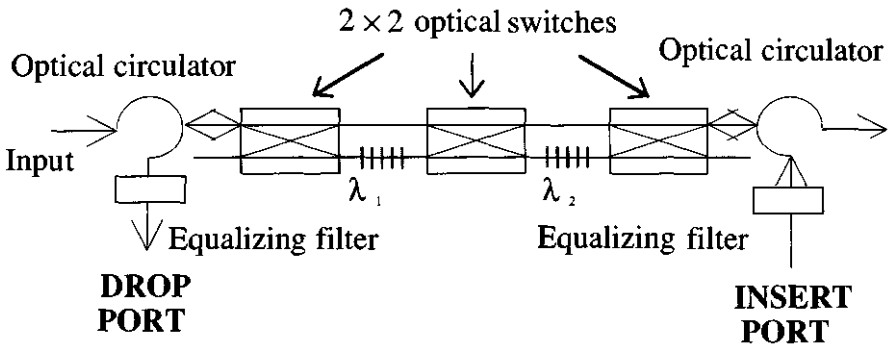

Figure 6.35: The reconfigurable optical add–drop multiplexer (ROADM) (after Ref. [67]).

circulators sandwich a set of optical cross-connect switches connected in series. Fiber gratings at the optical channel wavelengths are connected between one of the output ports of the cross-connect switches. This way, the incoming signals may be switched to the grating or bypass it. When switched to the grating, the channel at the grating wavelength λ_1 is dropped and routed to the drop port. All other channels proceed to the next switch, where the choice is repeated for the other channels. If, however, λ_1 bypasses the first grating, it goes on to the through port. The same applies to the other channels. At each two-by-two optical cross-point switch, a channel (or more, depending on the number of gratings between the switches) may be dropped. The ROADM is extremely flexible, allowing the node to be programmed relatively fast (<50 μs). The insertion loss of the optical switches is low (0.7 dB), and the device has been demonstrated as a two-channel ROADM [67], with a total insertion loss of 3 dB. The equalizing filters shown in Fig. 6.35 are intended to compensate for the loss of the switches and the gratings so that all channels suffer the same insertion loss.

A modification of the ROADM shown in Fig. 6.35 results in the simultaneous add–drop function, including automatic dispersion compensation of all channels, using dispersion compensating gratings (DCG) [68]. The channel dropping gratings are replaced by chirped dispersion compensating gratings. Uniform unchirped gratings can be used from either direction, whereas the dispersion of chirped gratings is reversed if it is turned around. Therefore, the chirped gratings cannot simply replace the unchirped gratings in the ROADM. Channels to be dropped are compensated for dispersion in the ROADM with DCGs. In order to dispersion compensate the "through" channels, the optical circuit has to be altered. The modified reconfigurable dispersion compensating ADM (RDC-ADM) is shown Fig. 6.36. The "through" channels are routed via the "through path" to the output circulator and reinjected into the cross-point switches. Each "through" channel is routed to the appropriate grating via the switches and dispersion compensated by reflection, to retrace the path to the circulator, and finally to the output. Channels are also inserted without reflection; they simply bypass the DCG allocated to their channel, so as to avoid the additional dispersion. The four-channel RDC-ADM was demonstrated with a 4×10 Gb/sec WDM system and used apodized 100-mm-long gratings for each channel designed to compensate for the dispersion of 8 km of standard fiber (1312 psec/nm). An important feature of the configuration was the arrangement of gratings and amplifiers to equalize the

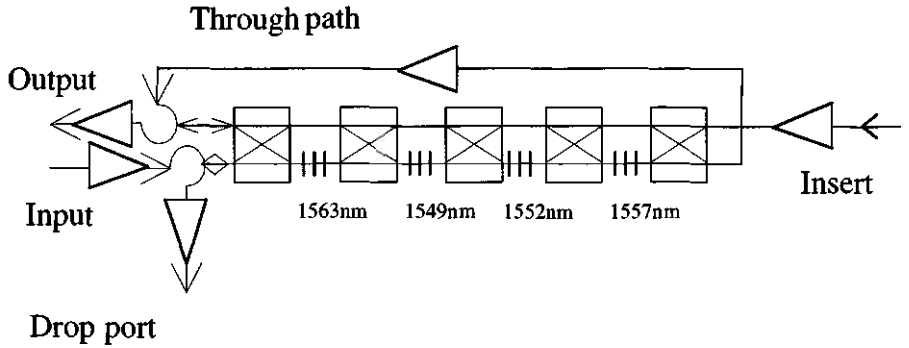

Figure 6.36: The RDC-ADM based on optical switches (after Ref.[68]).

insertion loss of the switches. The gratings are placed in the RDC-ADM such that the channel at the maximum gain of the amplifier is placed between the last pair of optical switches, and the lowest gain channel is reflected first [68].

6.6 The polarizing beam splitter band-pass filter

A filter based on an all-fiber polarization dividing coupler [69] changes the Michelson BPF into a noninterferometric device. The polarization splitting coupler allows only one of the orthogonally polarized eigenmodes to couple across to the other fiber. The coupler is fabricated to be an integral number of coupling lengths for one of the polarizations. Since the supermodes of the coupler have slightly different propagation constants, they have slightly different coupling lengths, $l_c(TE)$ and $l_c(TM)$, for the *TE* and *TM* polarized modes. By making the coupling region long, it can be arranged to be an odd number of coupling lengths for one polarization and an even number for the other. This ensures that only a single polarization couples across the coupler, while the other remains in the same fiber. Thus, the number of coupling lengths, N_c is

$$N_c \approx \frac{l_c}{\Delta l_c}, \tag{6.6.1}$$

where $\Delta l_c = |l_c(TE) - l_c(TM)|$, and $l_c \approx l_c(TE) \approx l_c(TM)$. As a result of

overcoupling, the device is wavelength sensitive, with a cyclic coupling response shown in Fig. 6.37. It has excellent polarization isolation over a narrow band of wavelengths but may be designed to operate at any desired wavelength by adjusting the parameters at the time of fabrication.

Figure 6.38 shows a schematic of the polarization splitting coupler in operation with Bragg gratings in ports 3 and 4. When operated at the correct wavelength, the polarization splitter will cross-couple only one of the two orthogonal polarization states in the input port 1, while the other propagates unaffected. If gratings are placed at the output ports of such a coupler, light at the Bragg wavelength is reflected and both polarizations are coupled back to the input port 1. If a quarter-wave plate is placed just before a grating and oriented such that at the output of the wave plate it is left-circularly polarized, on reflection from the grating it becomes right-circularly polarized. Traversing the wave plate once more the linearly polarized output of the wave plate is orthogonal to the incoming polarization. At the coupler, this state of polarization remains uncoupled and is routed to port 2 of the coupler. The same applies to the orthogonal polarization state, which also couples to port 2. Thus, as in the Michelson arrangement, the device operates as a polarization-*independent* band-pass filter [72]. Each

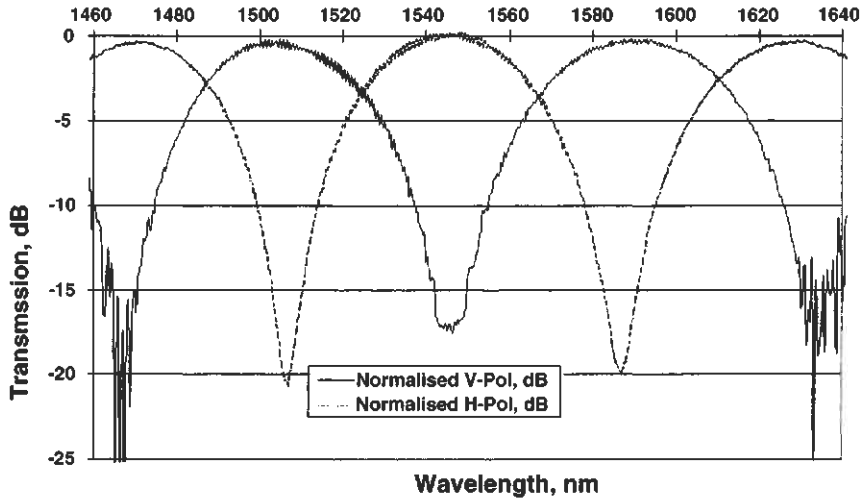

Figure 6.37: The transmission characteristics of the two orthogonal polarization states [72] at the output of the polarizing beam splitter. The extinction is well over 30 dB.

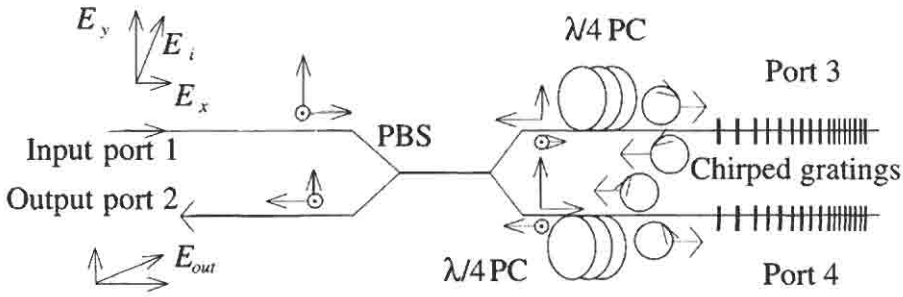

Figure 6.38: The polarization dividing band-pass filter in operation. The dashed arrows indicate the direction of propagation. The circles with arrows indicate the circularity of the polarization (after Ref [72]) PBS is a polarizing beam splitter. λ/4 PC is a quarter-wave polarization controller.

reflected polarization is routed to the output port of the coupler, reconstituting the original polarization, but is rotated by $\pi/2$.

The experimental arrangement using a cascade of four chirped gratings with two polarizing beam splitter band-pass filters (PBS-BPFs) is shown in Fig 6.39. The quarter-wave plates are simply a few turns of fiber in a polarization controller [70]. In this dispersion-compensating

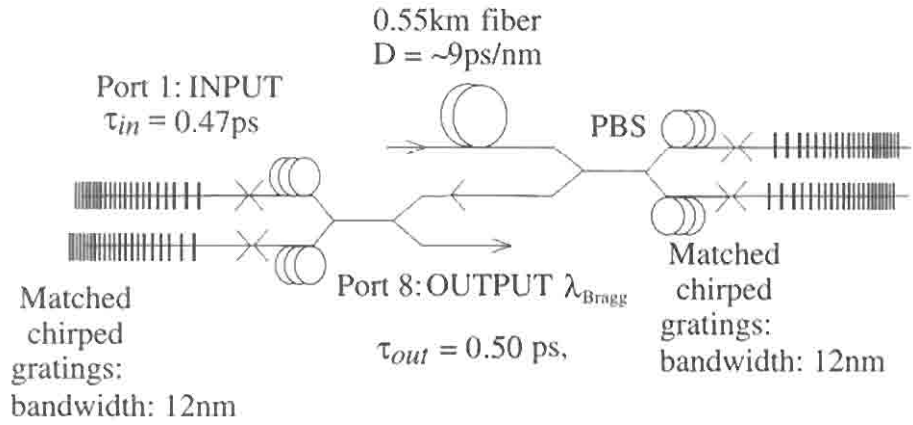

Figure 6.39: Dispersion compensation with four cascaded 8-mm-long, 12-nm bandwidth-chirped gratings and two PDBPF. The two polarization splitting band-pass filters shown here have been cascaded to enhance the dispersive effect of the chirped gratings [71,72].

PDBPF, 0.47-ps pulses at 1562 nm were stretched to 60 ps after propagation through 0.55 km of partially dispersion-shifted fiber (dispersion of 9 ps/nm). A pair of identical 8-mm-long chirped gratings with a bandwidth of 12 nm in the PDBPF routed the pulses to a second, identical DCG-PBS-BPF. The output port of the second PBS-BPF recovered pulses of 0.50 ps, a recompression ratio of 60/0.5 = 109 [72].

The PBS-BPF is a noninterferometric device but relies on the coincidence of the arrival of the pulses at the PDS after reflection. A delay between the arrival of the pulses translates into polarization mode dispersion (PMD). A change in the path of 1 mm is equivalent to ~10 ps PMD. For such short pulses, the paths were matched to <0.01 mm by stretching the fiber. Polarization variation in each arm causes an amplitude fluctuation. This device remains reasonably immune from physical disturbance, so long as the fibers after the PBS are not disturbed. Since all the components of this device are based on optical fiber, it has low insertion loss (~0.2 dB, typically, for the splitter).

The Michelson interferometer becomes the GMZI-ADM when a second coupler is included after the gratings. The same applies to the polarization dividing filter with a second PBS after the gratings. However, a major difference is the intrinsic stability of the latter device, since interferometer stability is no longer necessary. BER performance of transmission systems will degrade significantly as the PMD approaches half of the bit period. For a low BER at a transmission rate of 10 Gb/sec, a maximum path imbalance of a few millimeters would be required, which is easily achievable. The disadvantage of the filter is relatively small bandwidth of the PBS (see Fig. 6.36), so that channels can only be spaced close to the nulls of the PBS.

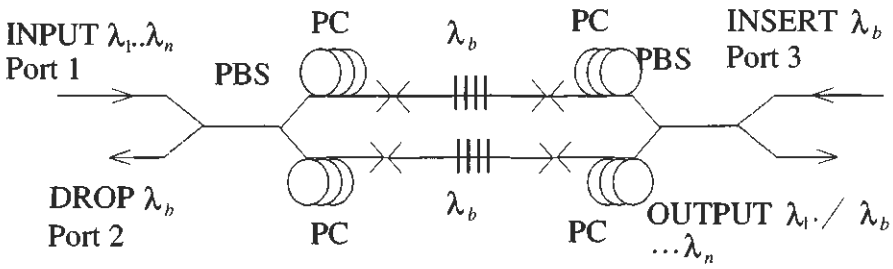

Figure 6.40: The polarizing beam splitter OADM. Multiple gratings between the PCs allow more than a single channel to be dropped and added simultaneously (after Ref. [73]).

A PBS-OADM has been demonstrated for a single channel using seven wavelengths spaced at 0.8-nm intervals. The center channel was dropped with a cross-talk penalty of 0.3 dB when the same wavelength was added at a transmission rate of 2.5 Gb/sec. Heating part of one arm of the PBS-OADM by 65°C induced a change of 0.3 dB at the output [73]. However, it remains to be seen how this device will function under full environmental testing. Figure 6.40 shows a schematic of the PBS-OADM [73].

6.7 In-coupler Bragg grating filters

Co- and contradirectional wavelength selective couplers have been known for a long time [74,75]. There are a number of ways that gratings in-couplers may be used to form band-pass filters. Figure 6.41 shows three different types of couplers, which include gratings to assist (grating-assisted coupler, GAC), to frustrate (grating-frustrated coupler, GFC) and to reflect (Bragg reflection coupler, BRC) light of a particular wavelength that meets the phase-matching requirements.

The period of the refractive index-perturbation for codirectional grating-assisted coupling [GAC, Fig. 6.41 (*i*)] between two dissimilar fibers is determined by the difference in the propagation constants of the two guides. This is generally small, and therefore the period is long. For weak overlap of the fields, the coupled-mode equations (see Chapter 4 on long-period gratings), describe the interaction between the modes. The coupling between the guides is sinusoidally periodic with length of the grating-assisted region. The coupling has a relatively broad bandwidth (tens of nanometers) and therefore poor wavelength selectivity, unless the device can be made very long.

A normally 100% coupler is strongly detuned by the dispersion of the grating and so fails to behave as a coupler near the Bragg wavelength, and is called a grating-frustrated coupler [GFC, Fig. 6.41 (*ii*)]. It works on the following principle: Two fibers with identical propagation constants will exchange power at all except the "grating-frustrated" wavelength. The in-fiber grating is a Bragg reflector at the frustrated-wavelength and is present in only one of the fibers. The far end of the input fiber becomes the "drop" port and is the one that does not contain the grating.

The Bragg reflecting coupler [BRC, Fig. 6.41 (*iii*) and (*iv*)] requires a perturbation with a short period, as is the case for Bragg reflection, being dependent on the sum of the magnitudes of propagation constants of

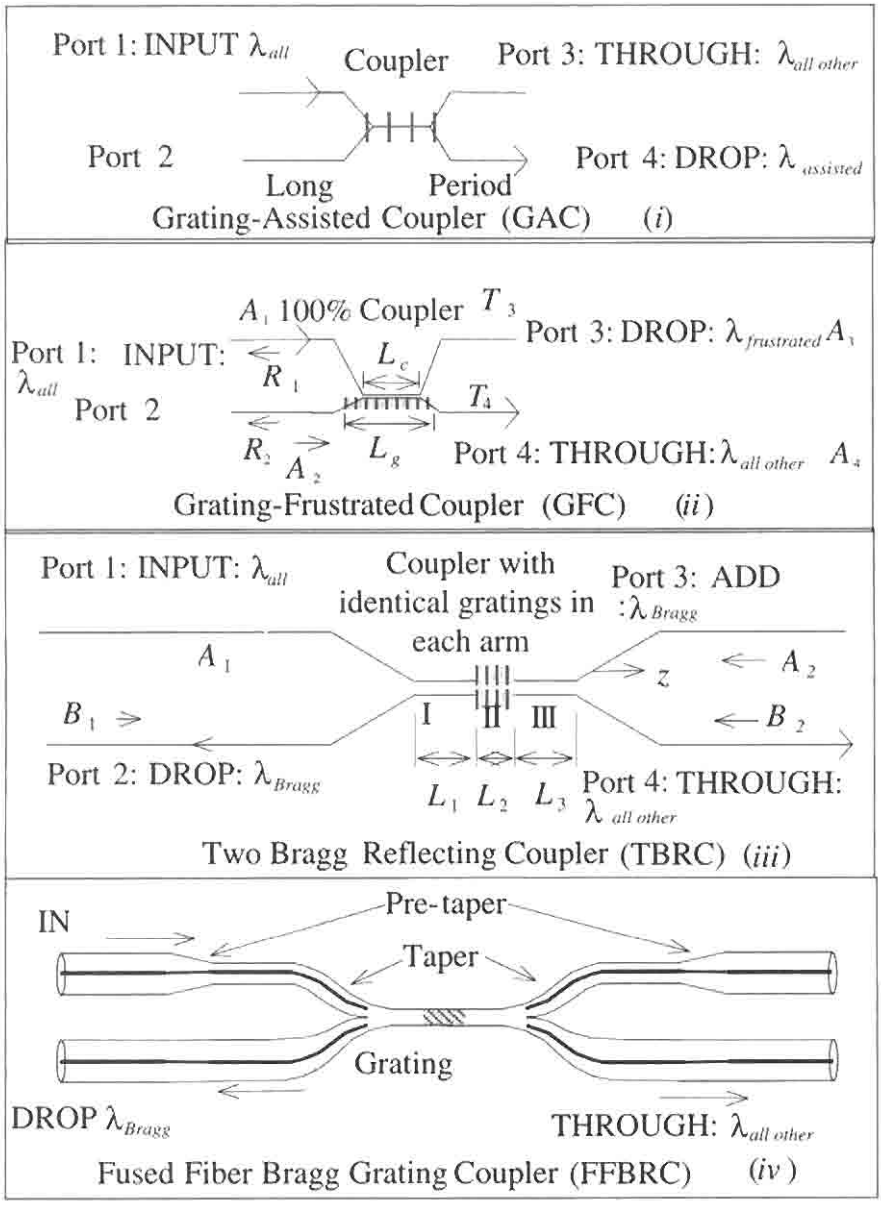

Figure 6.41: Some examples of band-pass filters with in-coupler gratings.

the two modes. This device can made with either two gratings in polished couplers [76,77] or a single one written into a fused coupler [78], since the perturbation has to be present in the entire cross-section of the coupling region. The dropped channel is reflected and routed to port 2 of the fiber coupler. In the following sections, the characteristics of the latter two devices are presented.

6.7.1 Bragg reflecting coupler OADM

The BRC-OADM [76–78] is probably the most promising of all the OADM devices that rely on interference. Essentially, this is a new twist to a range of generic devices based on the grating-assisted coupling action. Apart from being a simple device and having very low insertion loss, the BRC has the potential of fulfilling the requirements for a high extinction at the "dropped" as well as the "through" ports, and low back-reflection into the input port. Schematics of the BRC in the assembled and fused forms are shown in Fig. 6.41 (iii, iv). In its fused form, it comprises two fibers tapered down to form a long coupling region in which the fibers are kept parallel, followed by a short grating and another long coupling region before the fibers separate.

The principle of operation is probably the cleanest of all the different types of grating couplers and may be understood in the following phenomenological way: The light input into port 1 propagates adiabatically in the tapered region to excite the supermodes of the coupler. In this region, the two fibers merge into a single strand and become a glass rod without a core, surrounded by air. In a normal coupler without the grating, 100% of the light is transferred from one set of modes to the other to exit at port 4. If, however, a point reflector is placed at exactly half the coupling length, then the divided power between the modes travels backward toward ports 1 and 2, and the coupling process continues uninterrupted, apart from the π phase change induced by the reflection in all the supermodes. Thus, instead of propagation in the positive z-direction, the supermodes travel in the negative z-direction and interfere at the exit of the coupler and are routed by symmetry into port 2. In the BRC, the Bragg grating replaces the point reflector, which is wavelength selective, and routes light only near the bandgap into port 2. This simple picture is surprisingly accurate, despite the fact that coupling continues within the grating region, due to light penetration. It is immediately apparent that a strong grating would be preferable, although complications arise since the presence of the grating detunes the coupling action. The BRC can also be considered to be a close analog to the

Michelson/Mach–Zehnder interferometer with "zero-length" paths. This will become clear as one compares the theoretical performance of the BRC with that of the Michelson with *detuned* Bragg grating wavelengths. One essential difference between the two devices are the single grating as well as only one common path in the BRC, as opposed to two gratings and two paths in the Michelson interferometer. Many of the features of the BRC are easily understood by comparing it with the Michelson [79].

Theory of the BRC

The theory of the BRC has been worked out using coupled-mode analysis [76,80,77]. We closely follow the nomenclature of Ref. [77]. Referring to Fig. 6.41 (*iii*), the fibers and A and B have unperturbed propagation constants β_a and β_b, respectively, and the grating with a coupling constant of κ_{ac} exists in both fibers, evanescently coupled with a coupling constant κ. In region II, there are co- and counterpropagating modes, which are coupled together. The presence of the grating introduces a detuning of the propagation constants in each fiber, which are

$$\Delta\beta_a = \beta_a - \frac{\pi}{\Lambda_g} \tag{6.7.1}$$

$$\Delta\beta_b = \beta_b - \frac{\pi}{\Lambda_g} \tag{6.7.2}$$

$$\begin{aligned}\Delta\beta_{ab} &= \frac{1}{2}(\beta_a - \beta_b) \\ &= \frac{1}{2}(\Delta\beta_a - \Delta\beta_b).\end{aligned} \tag{6.7.3}$$

Coupling between counterpropagating modes of different fibers (A_1/B_2 and A_2/B_1) is only significant if the fibers are very strongly coupled, so that coupling occurs over a distance of a few wavelengths (when κ is of the order of $10^6 \mathrm{m}^{-1}$). Thus, these interactions can be ignored in a majority of cases. The mode fields propagate with the modified propagation constants and may be expressed as

$$A_1(z) = \tilde{A}_1(z)e^{i\Delta\beta_a z} \tag{6.7.4}$$

$$A_2(z) = \tilde{A}_2(z)e^{-i\Delta\beta_a z} \tag{6.7.5}$$

$$B_1(z) = \tilde{B}_1(z)e^{i\Delta\beta_b z} \tag{6.7.6}$$

$$B_2(z) = \tilde{B}_2(z)e^{-i\Delta\beta_b z}. \tag{6.7.7}$$

In region II, the coupled-mode equations take the matrix form

$$\begin{bmatrix} \tilde{A}_1' \\ \tilde{A}_2' \\ \tilde{B}_1' \\ \tilde{B}_2' \end{bmatrix} = \begin{bmatrix} -i\Delta\beta_a & -i\kappa_{ac} & -i\kappa & 0 \\ i\kappa_{ac}^* & i\Delta\beta_a & 0 & i\kappa \\ -i\kappa^* & 0 & -i\Delta\beta_b & -i\kappa_{ac} \\ 0 & i\kappa^* & i\kappa_{ac}^* & i\Delta\beta_b \end{bmatrix} \begin{bmatrix} \tilde{A}1 \\ \tilde{A}2 \\ \tilde{B}1 \\ \tilde{B}2 \end{bmatrix}, \tag{6.7.8}$$

where the prime indicates d/dz. Expressed as an eigenvalue equation, Eq. (6.7.8) results in the four eigenvalues (propagation constants) of the four supermodes of region II. These are arrived at by straightforward but tedious algebraic manipulation of Eq. (6.7.8) using standard techniques. The four eigenvalues are

$$\alpha_1 = \sqrt{|\kappa_{ac}|^2 - \left[\sqrt{|\kappa|^2 + \Delta\beta_{ab}^2} + \frac{\Delta\beta_a + \Delta\beta_b}{2}\right]^2} \tag{6.7.9}$$

$$\alpha_2 = \sqrt{|\kappa_{ac}|^2 - \left[\sqrt{|\kappa|^2 + \Delta\beta_{ab}^2} - \frac{\Delta\beta_a + \Delta\beta_b}{2}\right]^2} \tag{6.7.10}$$

$$\alpha_3 = -\sqrt{|\kappa_{ac}|^2 - \left[\sqrt{|\kappa|^2 + \Delta\beta_{ab}^2} + \frac{\Delta\beta_a + \Delta\beta_b}{2}\right]^2} \tag{6.7.11}$$

$$\alpha_4 = -\sqrt{|\kappa_{ac}|^2 - \left[\sqrt{|\kappa|^2 + \Delta\beta_{ab}^2} - \frac{\Delta\beta_a + \Delta\beta_b}{2}\right]^2}. \tag{6.7.12}$$

These are the most general solutions for the case when the fibers have different propagation constants. The eigenmodes associated with these eigenvalues have spatial fields that are expressed as the sum of individual modes of each fiber. The initial boundary values determine how each individual field grows (or decays). The first part of the analysis recognizes the fact that an input at either A_1 or B_1 results in coupling between the fibers through simple coupler action. This is described by the equation for the transfer function of the coupler [Eq. (6.3.1)], but with the appropriate coupling length, $L_c = L_1$, with input fields $A_1(0) = 1$ and $B_1(0) = 0$. At the boundary to the grating, the two fields $A_1(L_1)$ and $B_1(L_1)$ become the input to the grating. With the assumption that $A_2(L_1 + L_2) = 0$ and $B_2(L_1 + L_2) = 0$, the amplitudes of the four super-modes in region II are evaluated using Eq. (6.7.8). Finally, the backward propagating field amplitudes at the input to the coupler are propagated in reverse through the coupler to arrive at the amplitudes of the fields $A_2(0)$ and $B_2(0)$. Ideally,

with a point reflector (grating), the transmission through to the output ports would follow the equation for the coupler [Eq. (6.3.1a)], to route the entire out-off-band transmitted light to B_2. However, because of the finite length of the grating and the additional coupling that occurs in region II, region III may no longer be equal to region I for optimum performance, since $|\kappa|(L_1 + L_2 + L_3) = n\pi$.

As has been mentioned, a simple way of making such a device is to draw two identical fibers together to form a coupler and subsequently write a grating at the appropriate position, as shown in Fig. 6.41 (*iv*). With two fibers and two gratings, there is always a possibility of a small mismatch in the propagation constants after the fibers are polished and the device assembled. The refractive index mismatch maybe typically be $\sim 5 \times 10^{-5}$, resulting in ~95% coupling [38]. Gratings written into such fibers may therefore need to be written carefully in order to match the Bragg wavelengths. With a fused fiber coupler, the quality of the device can be very good with coupling approaching 100%, indicating the uniformity of the coupling region. Thus, assuming fibers with identical propagation constants, $\Delta\beta_{ab} = 0$, and the detuning $\Delta\beta_b = \Delta\beta$, simplifying Eqs. (6.7.9)–(6.7.12)

$$\alpha_1 = \sqrt{|\kappa_{ac}|^2 - (|\kappa| + \Delta\beta)^2} \tag{6.7.13}$$

$$\alpha_2 = \sqrt{|\kappa_{ac}|^2 - (|\kappa| - \Delta\beta)^2} \tag{6.7.14}$$

$$\alpha_3 = -\sqrt{|\kappa_{ac}|^2 - (|\kappa| + \Delta\beta)^2} \tag{6.7.15}$$

$$\alpha_4 = -\sqrt{|\kappa_{ac}|^2 - (|\kappa| - \Delta\beta)^2}. \tag{6.7.16}$$

Note that despite using phase-synchronous fibers, in Eqs. (6.7.13)–(6.7.16) the eigenvalues have been detuned from the exact phase-matching condition by κ.

To calculate the field at the input port 1 (return-loss) and the dropped port 2, the boundary conditions are applied. The dropped "transmission" in port 2 is

$$\tau_2 = \frac{B_2(0)}{A_1(0)} = \frac{1}{2}\frac{\kappa^*}{|\kappa|}\left[\frac{\kappa_{ac}^* \sinh(\alpha_1 L_2)}{i\alpha_1 \cosh(\alpha_1 L_2) + (\delta_1)\sinh(\alpha_1 L_2)} e^{-2i\phi} - \frac{\kappa_{ac} \sinh(\alpha_2 L_2)}{i\alpha_2 \cosh(\alpha_2 L_2) + (\delta_2)\sinh(\alpha_2 L_2)} e^{2i\phi}\right], \tag{6.7.17}$$

where the detuning, $\delta_1 = -|\kappa| - \Delta\beta$, $\delta_2 = |\kappa| - \Delta\beta$ and $\phi = (|\kappa| + \Delta\beta)L_1$.

Similarly, the back-reflected amplitude in port 1 is deduced as

$$\rho_1 = \frac{A_2(0)}{A_1(0)} = \frac{1}{2}\left[\frac{\kappa_{ac}^* \sinh(\alpha_1 L_2)}{i\alpha_1 \cosh(\alpha_1 L_2) + (\delta_1)\sinh(\alpha_1 L_2)} e^{-2i\phi} + \frac{\kappa_{ac} \sinh(\alpha_2 L_2)}{i\alpha_2 \cosh(\alpha_2 L_2) + (\delta_2)\sinh(\alpha_2 L_2)} e^{2i\phi}\right]. \tag{6.7.18}$$

We note that in Eq. (6.7.17) and (6.7.18), there are four terms of interest. The two terms in brackets can be immediately recognized to be identical to the reflectivity of two gratings at different Bragg wavelengths [see Eq. (4.3.11)], given by equating δ_1 and δ_2 to zero. Secondly, the phase term, 2ϕ, has two components; the first is due to the difference in the propagation constants of two modes propagating through a fiber of length, L_1, after being reflected by the grating. The second part, κL_1, is simply the accumulated phase change due to the coupling action of the coupler. The equivalent reflectivity and phase factors of two gratings as in Eq. (6.3.2) can replace the two terms within the square brackets of Eqs. (6.7.17) and (6.7.18):

$$\rho_1 e^{i\phi_1(\lambda)} = \frac{\kappa_{ac}^* \sinh(\alpha_1 L_2)}{i\alpha_1 \cosh(\alpha_1 L_2) + (\delta_1)\sinh(\alpha_1 L_2)}$$
$$\rho_2 e^{i\phi_2(\lambda)} = \frac{\kappa_{ac} \sinh(\alpha_2 L_2)}{i\alpha_2 \cosh(\alpha_2 L_2) + (\delta_2)\sinh(\alpha_2 L_2)}. \tag{6.7.19}$$

We note that the magnitude of the reflectivity $\rho_1 = \rho_2$, since it is the same grating with identical parameters, only different detuning. The dropped transmission in Eqs. (6.7.17) and (6.7.18) may be further simplified to

$$\tau_2 = \frac{1}{2}\rho_1[e^{i[\phi_1(\lambda)-2\phi]} - e^{i[\phi_2(\lambda)+2\phi]}]$$
$$\rho_1 = \frac{1}{2}\rho_1[e^{i[\phi_1(\lambda)-2\phi]} + e^{i[\phi_2(\lambda)+2\phi]}], \tag{6.7.20}$$

from which the power transmittance T_2 and back-reflectance R_1 are

$$T_2 = \frac{\rho_1^2}{2}[1 - \cos\delta] \tag{6.7.21}$$

$$R_1 = \frac{\rho_1^2}{2}[1 + \cos\delta], \tag{6.7.22}$$

where

$$\delta = \phi_1(\lambda) - \phi_2(\lambda) + 4|\kappa|L_1. \tag{6.7.23}$$

Interestingly, Eqs. (6.7.21) and (6.7.22) are exactly the same form as Eqs. (6.3.7) and (6.3.8), which describe the transfer characteristics of the *Michelson* interferometer with identical reflectivities but Bragg detuned gratings. In the BRC, the detuning is implicit in the phase factors ϕ_1 and ϕ_2 and calculated by equating δ_1 and δ_2 to zero, so that

$$\lambda^{1,2}_{Bragg} = 2n_{eff}\Lambda_g \frac{\pi}{\pi \pm \Lambda_g|\kappa|}, \tag{6.7.24}$$

where the sign in the denominator determines the perturbed Bragg wavelength of the slow, symmetric (negative sign) and fast (positive sign) antisymmetric supermodes. Note that for weak coupling, i.e., when $|\kappa| \to 0$, the splitting in the Bragg wavelength tends to zero. The detuning is *solely* dependent on the coupling constant of the coupler. For a given detuning, $2\Delta\lambda = \lambda^2_{Bragg} - \lambda^1_{Bragg}$, we can calculate the coupling constant by solving Eq. (6.7.24) as

$$|\kappa| \approx 2\pi n_{eff} \frac{\Delta\lambda}{(\lambda_{Bragg})^2}, \tag{6.7.25}$$

where λ_{Bragg} is the unperturbed Bragg wavelength.

Since the functional form of the properties of BRC band-pass filters are almost identical to that for the Michelson interferometer, the detuning that can be tolerated for low back reflection has been discussed in Section 6.3. For a back reflection of approximately -30 dB (requiring a detuning of $\sim$0.01 nm), we calculate the coupling constant $\kappa < 26\ \text{m}^{-1}$. This low value of the coupling constant is necessary to suppress the reflections on each side of zero detuning, as shown in Fig. 6.20. In a practical device, there is additional "apodization" due to the variation in the coupling constant in the tapered or curved region of the coupler, which will also tend to reduce the back-reflected light. For minimum back reflection, we note that T_1 in Eq. (6.7.20) is zero, so that the coupling length L_1 may be calculated as

$$L_1 = \frac{\pi + \phi_2(\lambda) - \phi_1(\lambda)}{4|\kappa|}. \tag{6.7.26}$$

Thus, for a low back reflection, the propagation constants of the fibers need to be matched carefully, as well as the Bragg wavelengths of the

gratings in each fiber. Fusing two fibers together creates a highly uniform taper with excellent physical symmetry. A fused coupler with a grating therefore has the potential of functioning as a device with the required characteristics.

A variant on the fused taper device is shown in Fig. 6.41 (*iv*), which relies on the propagation constants of the two fibers being *different* [78]. However, the overlap of the modes and the grating becomes very large, since the grating is in the entire waist region of the couple, and the fields are bounded by air. A tilted grating will therefore act as a mode converter when the Bragg matching condition is met,

$$\beta_1 + \beta_2 = \frac{2\pi}{\Lambda_g}, \tag{6.7.27}$$

where β_1 and β_2 are the propagation constants of the two odd and even modes.

This device has been demonstrated by Kewitsch *et al.* [78] with two identical fibers, one of which is pretapered as shown in Fig. 6.41 (*iv*) to change the propagation constant. A grating written in the waist at 1547 nm "dropped" 98% of the light in a bandwidth of 0.7 nm with a reported insertion loss of 0.1 dB. One problem with a fused taper device is the coupling to radiation modes of the fiber on the short-wavelength side of the Bragg wavelength, which can cause both cross-talk and loss.

6.7.2 Grating-frustrated coupler

The generic form of this device is shown in Fig. 6.41 (*ii*). The coupler consists of two fibers, which are assumed to be parallel, and a single Bragg grating is present in one waveguide alone. The grating-frustrated coupler can be modeled in several ways. These methods include supermodes of the structure [80,76] or using the coupled-mode theory developed by Syms [81]. Syms's model applies to a grating in both regions of the coupler and so has to be modified. In the following, the latter approach has been taken to model this device.

The analysis is in two stages as in the analysis of Bragg gratings: First, synchronous coupling is considered alone, i.e., at the Bragg-matched wavelength, and then the detuned case is analyzed.

For synchronous operation, both fibers have identical effective mode indexes at the Bragg wavelength: We ignore the perturbation introduced

by the grating. The evanescent fields of the two fibers overlap and an exchange of energy takes place.

The coupler can be analyzed by considering four modes with amplitudes $A_{1\ldots4}$. Mode 1 travels in the positive z-direction (from left to right) in the upper fiber, from $z = 0$ to $z = L$. Mode 2 also propagates along the positive z-direction in the lower fiber, from $z = 0$ to $z = L$. Mode 3 propagates in the negative z-direction in the upper fiber, from $z = L$ to $z = 0$. Last, mode 4 also propagates in the negative z-direction in the lower fiber, from $z = L$ to $z = 0$. The evolution of the mode amplitudes of the four waves is then described by a set of four first-order coupled differential equations.

There are three significant interactions that need to be considered:

1. Copropagating interactions between the modes of different waveguides (modes 1 and 2 as well as 3 and 4), as they do in a normal coupler without a grating. The overlap of the mode evanescent fields allows an exchange of energy to take place since the guides are phase matched. Because of symmetry considerations, a single coupling coefficient κ [Eq. (6.3.1c)] can be used.
2. Counterpropagating interaction between the modes of the same fiber. Modes 1 and 3, and 2 and 4, interact because of presence of the Bragg grating. The general form of the refractive index modulation of the grating, which allows this coupling, is given by Eq. (4.2.27). The phase mismatch is

$$\Delta\beta = \beta_1 + \beta_2 - \frac{2\pi N}{\Lambda_g}, \tag{6.7.28}$$

where the moduli of the mode propagation constants for the forward- and counterpropagating modes 1 and 2 are

$$\beta_1 = \beta_2 = \frac{2\pi n_{eff}}{\lambda}. \tag{6.7.29}$$

The phase-matched condition determines the optimum coupling between the forward- and backward-propagating modes when $\Delta\beta = 0$, at the Bragg wavelength. The presence of the grating promotes coupling between modes 2 and 4 since the grating is only in the lower waveguide, while modes 1 and 3 remain uncoupled. The coupling coefficient κ_{ac} for Bragg reflection is given by Eq. (4.3.6),

$$\kappa_{ac} = \frac{\pi\eta\overline{\Delta n}}{\lambda}. \tag{6.7.30}$$

3. We assume that there is no coupling between modes 1 and 4, 4 and 1, 2 and 3, and 3 and 2.

Taking the above considerations into account, the four coupled-mode equations which describe the coupling are

$$\begin{aligned}
\frac{dA_1}{dz} &= -i\{\kappa_c A_2\} \\
\frac{dA_2}{dz} &= -i\{\kappa_c A_1 + \kappa_{ac} A_4\} \\
\frac{dA_3}{dz} &= i\{\kappa_c A_4\} \\
\frac{dA_4}{dz} &= i\{\kappa_{ac} A_2 + \kappa_c A_3\}.
\end{aligned} \tag{6.7.31}$$

A similar procedure is followed as in the BRC coupler, and applying the boundary conditions results in the outputs of the device [82]. The grating-frustrated coupler works best when port 1 is excited (the fiber without the grating) with the grating extending along the entire coupling length and beyond, and with a coupler $\kappa L_c = \pi/2$. With this value of coupling, 100% of the power is transferred from one fiber to the other at a wavelength far removed from the Bragg condition, i.e., the device functions as a normal coupler. On-Bragg, the frustrated coupling depends on the strength of the grating coupling constant. The dependence of the transmission and reflection characteristics for port 1 excitation on the grating coupling strength is shown in Fig. 6.42.

Figure 6.43 shows the theoretical performance of a device similar to the one reported by Archambault *et al.* [83], with approximately 70% in the dropped port. Note that with increasing κL_c (over the coupling length), the on-Bragg wavelength transmission approaches unity, and the reflected power tends to zero. In practice, in-fiber gratings are limited to index modulations of $\sim 10^{-3}$, resulting in $\kappa L_c \approx 10$ for a coupling length of ~4 mm. Thus, the performance of this device is likely to remain limited, however elegant the principle, since the return loss remains high and dropped power will suffer a loss of ~1 dB, despite the insertion loss being intrinsically low (0.2 dB).

Figure 6.44 shows the transmission characteristics of a GFC with a $\kappa_{ac} L_c = 9$ ($\delta n = 2.75 \times 10^{-3}$, and $L_c = 1.57$ mm). The FWHM bandwidth is in excess of 4 nm, the pass-band transmission is >0.9, and the transmis-

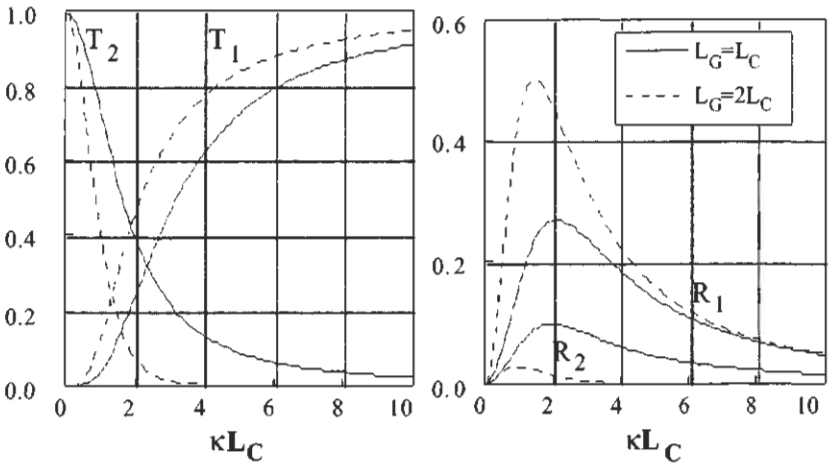

Figure 6.42: Transmission and reflection characteristics for the GFC as a function of the strength of the grating (courtesy Philip Russell from: Archambault J.-L., Russell P. St. J., Barcelos S., Hua P., and Reekie L., "Grating frustrated coupler: a novel channel-dropping filter in single-mode optical fiber,"*Opt. Lett.* **19**(3), 180–182, 1994. Ref. [83]).

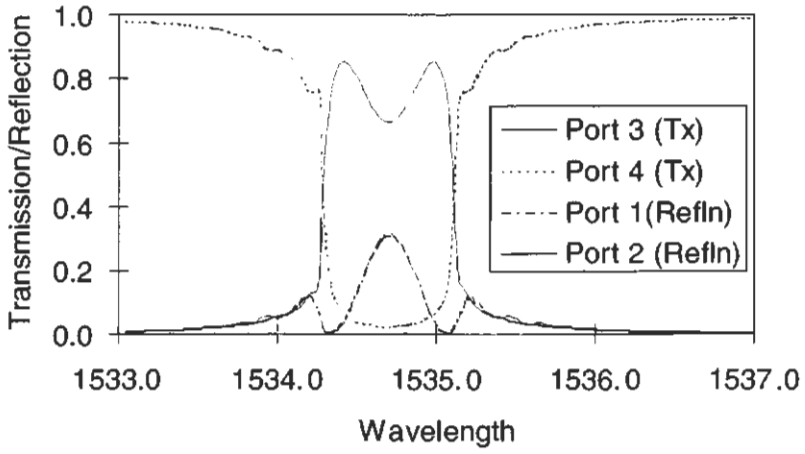

Figure 6.43: Transmission and reflection characteristics of a GFC. Simulation for L_c = 2.5 mm, L_g = 4.5 mm, $\delta n = 3 \times 10^{-4}$, n_{eff} = 1.45. λ_{Bragg} = 1534.7 nm (from: Wolting S., "Grating frustrated couplers," BT Research Laboratories Summer Studentship Report, 1995. Ref. [84]).

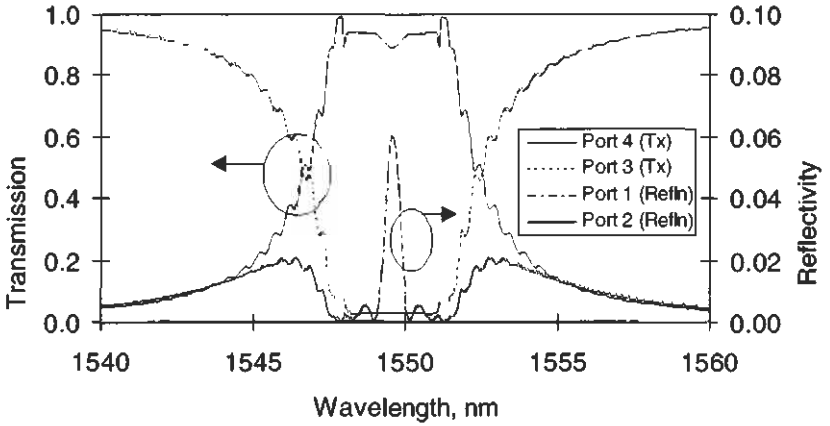

Figure 6.44: The transmission characteristics of the four ports of GFC with a $\kappa_{ac}L_c = 9$, $\delta n = 2.75 \times 10^{-3}$, and $L_c = L_g = 1.57$ mm (from Ref. [84]).

sion in the stop band is still of the order of ~0.05. As an OADM, this device is unlikely to have the performance necessary for telecommunications applications.

6.8 Side-tap and long-period grating band-pass filters

The theory of radiation mode coupling can be found in Chapter 4. Radiation mode coupling is generally used in applications requiring a lossy filter. For example, in flattening the gain spectrum of an erbium-doped fiber amplifier, a multiple side-tap grating (STG) filter [85] and the long-period grating (LPG) [86] have both been successfully used to eliminate the large variations within the gain bandwidth. The light "lost" from the fiber through radiation mode coupling can be substantial, if the grating is strong. Side-tap blocking filters can attenuate ~100% of the light within a narrow band, which can be tailored to span 100 nm or more. While STGs in general allow coupling to *all* order modes (odd and even, LP_{mn}), untilted LPGs couple guided-mode light to only $m = 0$ order modes (LP_{0n}). Choice of blaze angle and the v-value of the fiber easily tailor the loss spectrum and bandwidth of the STG. The bandwidth of the LPG is determined by the coherent interaction between the radiated cladding mode

and the guided mode over the long grating length (centimeters), with a bounded cladding. With an unbounded cladding, the loss spectrum of the LPG becomes extremely wide (>100 nm) [87], since the dispersion in ($n_{\text{eff}} - n_{\text{cladding}}$) is very weak. Figures 6.45*a* and *b* show light exiting from the side of a fiber by an STG and an LPG. The cladding mode has a better chance of interacting with the LPG. A ray exiting the core at an angle of 10° to the fiber axis will travel ~0.4 mm before being reflected back toward the grating in a 125-μm diameter fiber. Shallower angle rays may miss the STG altogether after the first reflection at the cladding–air interface. This is less likely in the LPG, which may be 2–10 times longer than a typical STG. Therefore, there may be continual exchange of energy between the radiated mode and the guided mode with the LPG, unless the cladding is made "infinite" by applying index-matching oil to the cladding. Instead of coupling to discrete radiation modes (approximately the same as the cladding modes), light is coupled to a continuum of the radiation field, so that a broadband loss spectrum is seen in transmission rather than a narrow bandwidth of the cladding mode [87].

Note that the angular distribution of the radiation for the LPG as a function of wavelength is reversed compared to the STG; i.e., the longest wavelengths exit at the largest angle (see Chapter 4).

The basic principle of the coupling relies on the phase-matching conditions, and the overlap integrals determine the strength and the wave-

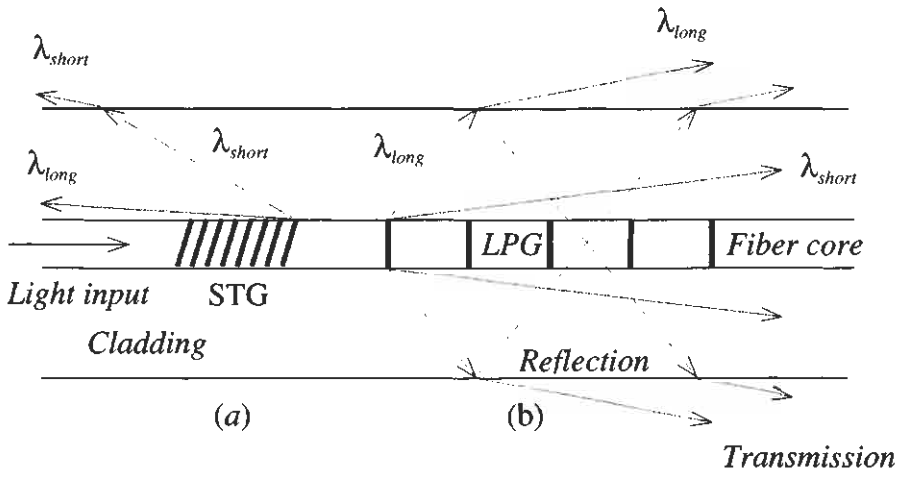

Figure 6.45: Light radiated from the STG and (b) from the LPG.

length dependence of the loss. There are two bounds to the loss spectrum, one on the short- and the other on the long-wavelength side: Light radiated out of the fiber core subtends a wavelength-dependent angle $\theta(\lambda)$ to the counterpropagation direction (STG) and copropagating (LPG), which depends on the inclination of the grating and period.

For the STG, this angle of the radiated light at wavelength λ in the infinite cladding is easily shown to be

$$\cos[\theta(\lambda)] = \frac{1}{n_{clad}}\left(\frac{\lambda}{\Lambda_g} N \cos\,\theta_g - n_{eff}(\lambda)\right), \tag{6.8.1}$$

where θ_g is the tilt of the grating with respect to the propagation direction, and N is the order of the grating. The angle at which the light exits from the side of the fiber varies as a function of wavelength and therefore can be used as a band-pass filter. The bandwidth of the radiated light can be shown to be approximately

$$\Delta\lambda \approx \frac{\Lambda_g \sin^2(\theta_g)}{2\cos(\theta_g)}. \tag{6.8.2}$$

However, the phase-matching condition alone does not determine the peak wavelength, in the general case when the grating is titled; the overlap integral together with the phase matching alters the spectrum and shifts the wavelength of maximum loss (see Chapter 4). Typical transmission loss and reflection spectra for a strong STG are shown in Fig. 6.46a, and

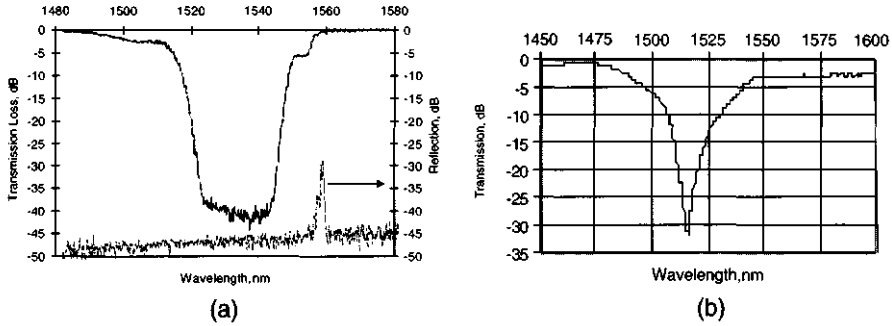

Figure 6.46: The transmission loss (and reflection) of (a) a 4-mm-long side-tap grating filter and (b) LPG filter with a 400-micron period, both written in a boron–germania codoped fiber.

the transmission loss spectrum of an LPG, in Fig. 6.46b. Both gratings were written in the same fiber.

The STG has been used as a spectrum analyzer by Wagener *et al.* [88]. A chirped grating blazed at 9° to the propagation direction was used to out-couple light from a fiber. The chirped grating had a decreasing period away from the launch end of the fiber. Since the angle $\theta(\lambda)$ subtended by the radiated light at a wavelength λ becomes smaller with reducing pitch [Eq. (6.8.1)], the focus of the light coupled out at different points is a function of the wavelength. The focal length is inversely proportional to the wavelength of the radiated light as [88]

$$f(\lambda) = \frac{\Lambda_g^2}{\cos(\theta_g)} \frac{L_g}{\delta\lambda_g} \frac{\sin[\theta(\lambda)]}{\lambda}, \tag{6.8.3}$$

where Λ_g is the nominal period of the chirped grating, n is the refractive index of silica, and L_g and $\delta\lambda_g$ are the length and the change in the period of the grating due to chirp (in nm), respectively. The radiated light was detected by a 256-element photodiode array, the center of which was arranged to be at the focus of the light at λ_c, the wavelength radiated by the center of the grating. A schematic of the device is shown in Fig. 6.47.

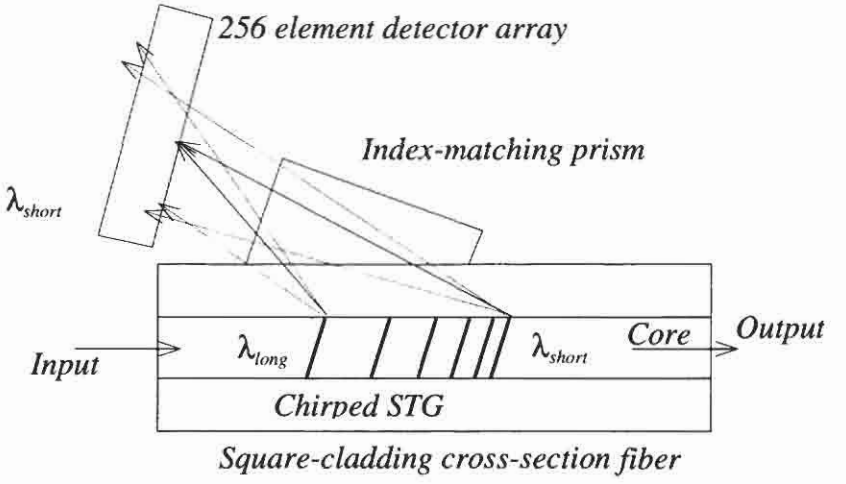

Figure 6.47: A schematic of the in-fiber chirped STG spectrum analyzer (after Ref. [88]).

A weak, 20-mm-long grating (Δ_g = 547 nm) with a chirp in the period of 1.92 nm (±0.96 nm) was used to tap ~5% of the light over a 35-nm bandwidth. An index-matched prism was placed in contact with a fiber of square cladding cross-section to promote good adhesion, to direct the light to the photodiode array.

The effective focal length was 160 mm. The resolution of the spectrometer was demonstrated to be 0.12 nm with a measured bandwidth of 14 nm, an insertion loss of <1 dB, a wavelength accuracy of ±0.03 nm, a power level accuracy of <0.25 dB, and a dynamic range of 35 dB. The spectrum of two resolved channels separated by 50, 100, and 200 GHz using this spectrometer is shown in Fig. 6.48 [88].

While this device is an excellent example of a band-pass filter, which is also tunable, the applications of the STG and the LPG in this area

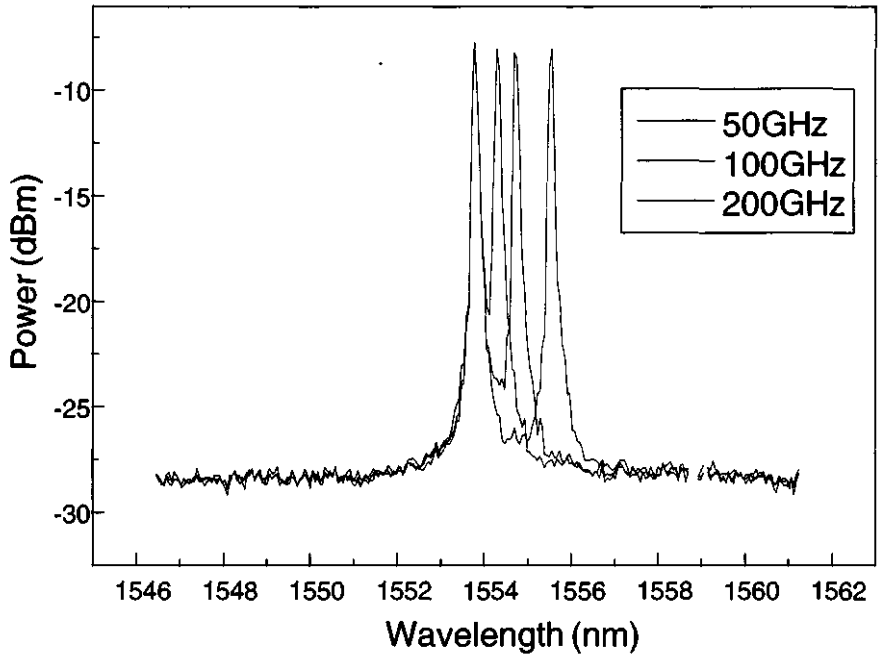

Figure 6.48: The spectrum of two channels as the detuning is increased from 50 to 100 to 200 GHz (courtesy T. Strasser, from Wagener J. L., Strasser T. A., Pedrazzani J. R., and DeMarco J., "Fiber grating optical spectrum analyzer tap," *In Tech. Digest of ECOC'97, Publn. No. 448*, Vol. 5, pp. 65–68. © IEE 1997 Ref. [88]).

have not really been exploited. It is envisaged that supervisory operations of fiber amplifiers is another possible application in which the filter that attenuates the spectrum can allow the monitoring of the performance and control of the amplifier characteristics.

6.9 Polarization rocking band-pass filter

Another type of band-pass filter is the polarization-converting filter. Much of the earlier work focused on the study of photoinduced polarization effects and fabrication of internally written filters [89–95]. The polarization sensitivity of fiber was recognized early in the development of photosensitive phenomena [96]. Birefringence can be photoinduced in Ge-doped fibers [97] because of preferential bleaching of defects [89]. Coupling between orthogonal polarizations was shown in elliptical core fibers due to dynamic changes in the birefringence [98]. A novel *counterpropagating* polarization coupling filter has also been reported, using internally written gratings [99]. It was shown that stress birefringence can be reduced in elliptical cored fibers illuminated with UV radiation [100]. Thus, in principle, the control of the birefringence by external means allows the fabrication of polarization coupling devices at any wavelength. In this section, we consider externally written filters, which can be fabricated for operation at any desired wavelength.

The theory of coupling between polarization can be found in Chapter 4. The band-pass filter functions by rotating the polarization of the input mode by $N\pi/2$. In order to discriminate between the two states, a polarizing component has to be used. A schematic of the filter is shown in Fig. 6.49.

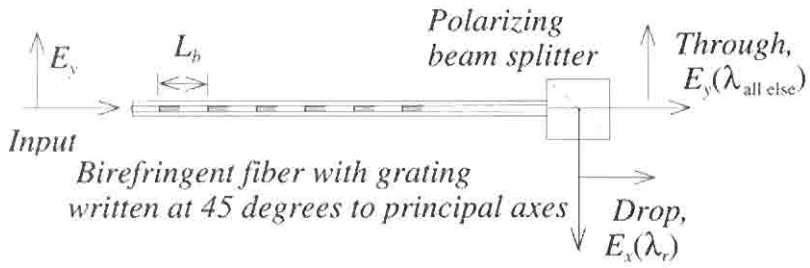

Figure 6.49: The polarization rocking "drop" filter.

Two types of polarization rocking filters can be fabricated. Birefringent polarization maintaining fiber can be used with a given predetermined beat length [101], or nonbirefringent fibers, which are deliberately made birefringent, may also be used [102]. In the first case, *Hill et al.* [101] showed that a filter with only 85 periods had a polarization conversion efficiency of 89% at a wavelength of 1292 nm in a FW bandwidth of ~8 nm. The filter length was reported to be 0.87 m, fabricated in an Andrew Corp. fiber with a birefringence $B = 1.27 \times 10^{-4}$. The transmission spectrum of this filter is shown in Fig. 6.50. The narrow bandwidth is a direct result of the high birefringence of the fiber. Apodized filters have also been demonstrated using the same principle, but with a grating coupling constant which is weighted as a function of length [103]. For the filter to function properly, care needs to be taken, since the input polarization has to remain stable.

In the second type of filter, a nonbirefringent fiber is wrapped on a cylinder to impart a known birefringence [104] (see Chapter 3). Given that the birefringence can be controlled, the beat length and therefore the rocking period is known. This methods allows the fabrication of very

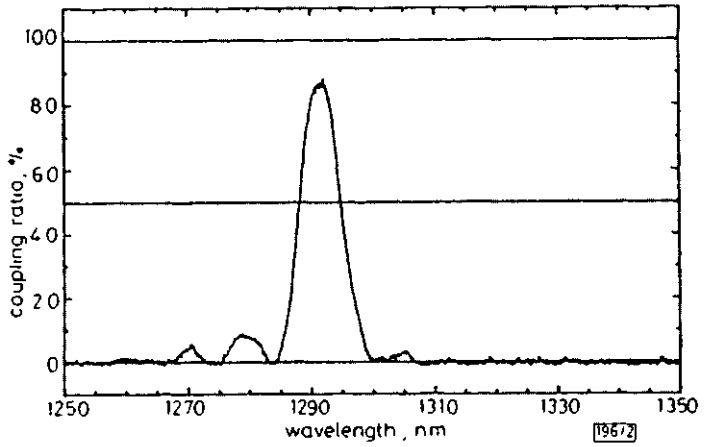

Figure 6.50: Transmission spectrum of an 85-step, polarization-rocking filter fabricated in a polarization maintaining fiber (from: Hill K. O., Bilodeau F., Malo B., and Johnson D. C., "Birefringent photosensitivity in monomode optical fibre: application to external writing of rocking filters," *Electron. Lett.* **27**(17), 1548, 1991. © IEE 1991. Ref. [101]).

long fiber filters, since the bend-induced birefringence is small (beat length ~0.75 m at 1550 nm) even with the tightest tolerable bend in standard telecommunications fibers [102]. The reported filter had a polarization coupling efficiency of ~100% at a peak wavelength of 1540 nm, with a FW bandwidth of 130 nm, in a filter that was only 17 beat lengths long (L_r = 10.89 m), with 27% of each beat length exposed to UV radiation (duty cycle of 27%).

The bandwidth of these filters between the first zeroes of the transmission spectrum follows from Eq. (4.4.12) as

$$\alpha L = \pm \pi, \tag{6.9.1}$$

so that the bandwidth, $2\Delta\lambda$, from Eq. (4.5.11)

$$2\Delta\lambda = \frac{2\pi\lambda L_b}{L_r}. \tag{6.9.2}$$

The fabrication of the rocking filter depends on the periodic exposure to UV radiation of *half* of the beat length of the fiber. This induces a refractive index modulation, which is only half of what it would be if the second half of the beat length was modulated by a *negative* index change, or if the rocking of the birefringence was truly $\pm\phi$ per beat length. This has the beneficial effect of halving the filter length L_r. This is particularly useful, because the rocking angle ϕ saturates at approximately 0.4°–0.5° per beat length with exposure to many pulses [105]. In order to overcome this problem, Psaila *et al.* [105] used a double pass scheme to double the rocking angle per beat length. In the first pass, the fiber was exposed at 45° to the birefringent axes, half of each beat length of 14 mm. The stationary fiber was exposed to a moving, pulsed UV beam through a 0.5-mm slit, with the UV polarization orthogonal to the fiber propagation axis. On the second scan, the fiber was rotated by 90° around the propagation axis, and the other half of the beat length was exposed in a similar manner. The result is the doubling of the rocking angle per beat length, leading to a rocking filter with ~98% conversion efficiency, only 33 beat lengths long, and with a FWFZ (full width to first zeroes) bandwidth of 20 nm.

It should be noted that the polarization coupler is a band-pass filter in transmission and that it converts either input polarization to its orthogonal state. As a consequence of this, a concatenation of two such filters results in a Mach–Zehnder type interferometer [106]. A schematic of this

filter is shown in Fig. 6.51. The transmitted output intensity can be shown to be [106]

$$I = \left(\frac{\kappa_{ac}^2}{\alpha^2}\sin^2\alpha L_r\right)\left[\cos^2\alpha L_r + \frac{\Delta\beta^2\sin^2\alpha L_r}{4\alpha^2}\right][1 + (1 + L_s)\cos(kB)], \qquad (6.9.3)$$

where $k = 2\pi/\lambda$, L_r is the length of the rocking filter, L_S is the distance between the two filters, $\kappa_{ac} = \Delta n/\lambda_r$, and B is the birefringence, $n_x - n_y$. The detuning parameter $\Delta\beta = \beta_x - \beta_y - 2\pi/\lambda$, with the usual definition of α (see Chapter 4). If the filter separation $L_s < L_{coh}L_b/\lambda$, where L_{coh} is the coherence length of the source, then strong interference is visible at the output.

Kannellopoulos *et al.* [106] fabricated the filter in Andrew Corp D-fiber with a polarization beat length of 4.35 mm (L_b) at a wavelength of 780 nm and $B = n_x - n_y = 1.8 \times 10^{-4}$. The core-to-cladding index difference was 3.3×10^{-2} with a higher mode cutoff of 710 nm. The rocking filters centered at 787 nm were 224.4 mm long (L_r) and separated by 320 mm (L_s). The period of the gratings was 4.4 mm, and they were written with 266-nm wavelength pulsed radiation, exposed to 2400 pulses at a peak intensity of 1.4 MW/cm^2. Each filter had a coupling efficiency of 7.5% so that the peak refractive index modulation $\delta\Delta n' = 9.7 \times 10^{-7}$. Figure 6.52 shows the transmission characteristics of the polarization coupling MZI. The output shows three peaks in transmission, each with a FW bandwidth of ~8 nm. The temperature sensitivity of the resonant wavelength of the filter is high (0.5 nm/°C) compared to that of Bragg gratings (0.006 nm/°C), and so the filter is suited to sensing temperature. When one of the filters is heated, the resonant wavelength shifts; alternatively, heating the section between the couplers influ-

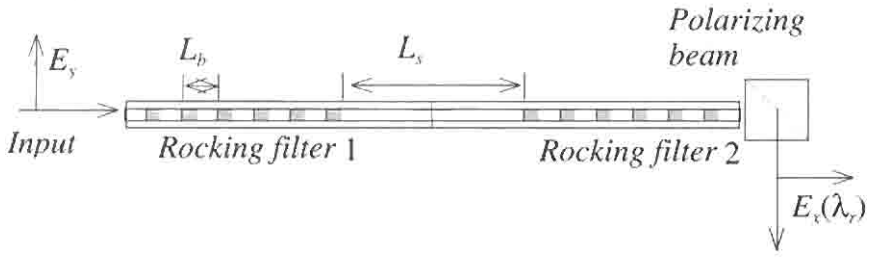

Figure 6.51: The polarization rocking Mach–Zehnder band-pass filter fabricated in birefringent fiber with two gratings written at 45° to principal axes (after Ref. [106]).

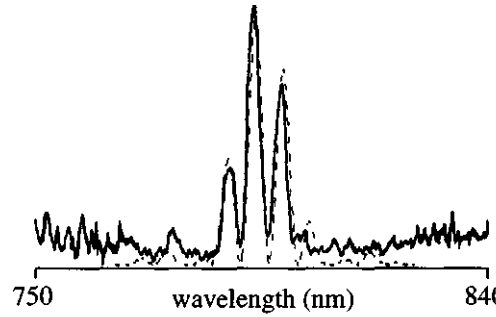

Figure 6.52: The transmission characteristics of the polarization coupling Mach–Zehnder interferometer (Courtesy S. Kannellopoulos, from: Kanellopoulos S. E., Handerek V. A. and Rogers A. J., "Compact Mach-Zehnder fibre interferometer incorporating photo-induced gratings in elliptical core fibers," *Opt. Lett.* **18**(12), 1013-1015, 1993. [106]).

ences the output state, from which a phase sensitivity of ~0.22 rad/°C was calculated over a temperature range of 150°C.

6.10 Mode converters

Mode converters work on a principle similar to that of the polarization converter. There are several types of mode-converting filters: those that couple one guided mode to another co- or counterpropagating guided mode, as well as those which couple a guided (or cladding) mode to a co- or counterpropagating cladding mode (or guided mode). Coupling of a guided mode to a co- or counterpropagating cladding mode has been partially covered in Section 6.8 on side-tap and long-period grating band-pass filters, and also in Chapter 4. Guided–guided co- and counterpropagating mode coupling devices will be discussed in this section. Other devices based on concatenated couplers for mode reconversion will also be discussed.

6.10.1 Guided-mode intermodal couplers

The theory of guided-mode coupling to both copropagating and counterpropagating guided/radiation modes can be found Chapter 4. Equations

(4.3.16), (4.4.11), and (4.4.12) govern the coupling of counter- and copropagating guided modes. Coupling of the modes of the same order is always possible, provided the phase-matching condition is met. The overlap integral, Eq. (4.4.5), for the coupling of dissimilar modes is zero, unless the transverse distribution of the refractive index modulation is not constant, breaking the symmetry. Thus, a slanted grating will increase the overlap integral between modes of different order, since the transverse refractive index modulation profile is no longer uniform. This was first reported by Park and Kim [107] using a novel internal mode-beat grating, by exciting a bimoded fiber at a wavelength of 514.5 nm from a CW argon laser. The beating of the modes automatically creates a blazed grating with the intensity of the laser radiation varying transversely across the core with the mode-beat period. This intensity grating induced a photoinduced grating, which created the mode converter. This principle has been extended by Ouellette [108] by recognizing that the phase-matching condition is met by more than one set of modes due to the nondegeneracy of the modes, but at longer wavelengths. Thus, a grating written at 488 nm by exciting a chosen pair of modes allowed the "reading" of the holographic grating at around 720 nm. Further experiments have demonstrated the sensitivity of the mode beat length to the applied strain [109], since the propagation constants of the fundamental and higher-order modes change differentially. These types of converters have applications in strain sensing and as nonlinear optical switches [110]. A phase-matching condition is also possible where the beat length $L_b \to \infty$ [111,112], allowing very long period gratings to be used.

A principle similar to the one reported by Park and Kim [107] has been used to fabricate mode converters at different wavelengths. The coupling between the LP_{11} and LP_{01} modes was made possible by slanting the grating using an external, point-by-point UV exposure technique [113], details of which may be found in Chapter 3.

A slit (12 μm) at an angle of 2–3° was used to expose the fiber at the first-order period of 590 μm ($N = 1$) mode beat length, $2\pi/[N(\beta_{LP01} - \beta_{LP11})]$, resulting in a mode converter at a wavelength of 820 nm in a Corning Telecommunications fiber with a higher-order mode cutoff of 1.1 μm [113]. The grating had typically 200–300 steps for 100% coupling, while overcoupled converters with 1000 periods were also reported. These convert the LP_{01} to the LP_{11} and then back again to the LP_{01}. Unlike polarization rocking filters, mode-converting gratings can be very strongly coupled, so that the side lobes of the *sinc* function in Eqs. (4.4.11) and

(4.4.12) become large with a large refractive index modulation, and multiple peaks can be seen in the transmission spectrum. A FWFZ of ~5 nm was observed. A higher-order mode stripper has to be used to observe the loss spectrum of this filter. For the band-pass function, the higher-order mode has to be selected. Alternatively, the higher mode can be excited preferentially in the overcoupled filter and stripped at the output so that the "dropped" wavelength is in the fundamental mode, with the through state in the LP_{11} mode.

Conversion from LP_{01} mode to the leaky counterpropagating LP_{11} mode has been observed in depressed-clad fibers in which tilted Bragg gratings were written [114]. In this case, the fiber supported the LP_{11} mode over short lengths, so that a "ghost" dip is observed in the transmission spectrum at a wavelength slightly shorter than the Bragg reflection wavelength. While the light is coupled into the LP_{11} mode, the reflection is not visible if the fiber on the input side of the gratings is mode stripped. Gratings with a tilt angle of 3° have been written in standard telecommunications fibers preexposed to raise the index to allow the LP_{11} mode to be supported [115] over the UV-exposed length. The overlap between the LP_{01} mode and the LP_{11} mode is almost the same as the LP_{01} mode for this tilt angle, so that efficient reflective mode coupling is possible. The side illumination induces a nonuniform refractive index change across the core, breaking the LP_{11} mode degeneracy and causing two reflections to occur. Depressed-cladding fibers have been examined by Haggans *et al.* [116] with a view to reducing the coupling to radiation and cladding modes.

Coupling to similar order modes does not require a transverse asymmetry in the grating (see Chapter 4). Therefore, the LP_{01} mode is coupled to the LP_{02} mode for both co- and contradirectional converters with a transversely uniform grating. The coupling constant κ_{ac} [117] is

$$\kappa_{ac} = \frac{\pi \Delta n}{\lambda} \left(\frac{w_{01} w_{02}}{v^2 (u_{01}^2 - u_{02}^2)} \right) \times \left(u_{01} \frac{J_0(u_{02})}{J_1(u_{02})} - u_{02} \frac{J_0(u_{01})}{J_1(u_{01})} \right), \tag{6.10.1}$$

where the subscripts refer to the mode, and u, w, and v are the normalized waveguide parameters defined in Chapter 4. The interaction of the $LP_{01} \rightarrow LP_{02}$ mode is particularly useful for narrow-band filters [118] and for broadband dispersion compensation [119]. In the latter application,

gratings between 27 and 35 mm long have been fabricated with periods ranging from 116 to 135 μm in few-moded fiber. Up to 85% coupling is obtained with a FWHM bandwidth of 25 nm. The step-chirped technique [120] can also be used to broaden the bandwidth for longer mode-converter gratings. A 65-mm-long grating with a 0.3-μm chirp over four sections has been demonstrated to have a peak coupling efficiency of 90% at 1556 nm and a FWHM bandwidth of 14 nm.

References

1. Haus H. A. and Shank C. V., "Anti-symmetric type of distributed feedback lasers," *J. Quantum Electron* **12**, 532–539 (1976).
2. Utaka K., Akiba S., and Matsushima Y., "1/4-shifted GaAsP/InP DFB lasers by simultaneous holographic exposure of negative and positive photoresists," *Electron. Lett.* **20**, 1008–1010 (1984).
3. Haus H. A. and Lai Y., "Theory of cascaded quarter wave shifted distributed feedback resonators," *IEEE J. Quantum Electron.* **28**(1), 205–213 (1992).
4. Zengerle R. and Leminger O., "Phase-shifted Bragg-grating filters with improved transmission characteristics," *J. Lightwave Technol.* **13**(2), 2354–2358 (1995).
5. Agrawal G. P. and Radic S., "Phase-shifted fiber Bragg gratings and their applications for wavelength demultiplexing," *IEEE Photon. Technol. Lett.* **6**, 995–997 (1994).
6. Kashyap R., McKee P. E., and Armes D., "UV written reflection grating structures in photosensitive optical fibres using phase-shifted phase-masks," *Electron. Lett.* **30**(23), 1977–1978 (1994).
7. Canning J. and Sceats M. G., "π-phase shifted periodic distributed structures in optical fibers by UV post-processing," *Electron. Lett.* **30**(16), 1244–1245 (1994).
8. Asseh H., Storoy H., Kringlebotn J. T., Margulis W., Sahlgren B., and Sandgren S., "10 cm long Yb^+ DFB fibre laser with permanent phase shifted grating," *Electron. Lett.* **31**, 969–970 (1995).
9. Loh W. H. and Laming R. I., "1.55 μm phase-shifted distribute feedback fibre laser," *Electron. Lett.* **31**(17), 1440–1442 (1995).
10. Hübner J., Varming P., and Kristensen M., "Five wavelength DFB fibre laser source for WDM systems," *Electron. Lett.* **33**(2), 139–140 (1997).
11. Zever I, *Handbook of Filter Synthesis*. Wiley, New York (1967).

12. Wei L. and Lit W. Y., "Phase-shifted Bragg grating filters with symmetrical structures," *IEEE J Lightwave Technol.* **15**(8), 1405–1410 (1997).

13. Bhakti F. and Sansonetti P., "Design and realization of multiple quarter-wave phase-shifts UV written bandpass filters in optical fibers," *IEEE J. Lightwave Technol.* **15**(8), 1433–1437 (1997).

14. Farries M. C., Sugden K., Reid D. C. J., Bennion I., Molony A., and Goodwin M. J., "Very broad reflection bandwidth (44 nm) chirped fibre gratings and narrow-bandpass filters produced by the use of an amplitude mask," *Electron. Lett.* **30**(11), 891–892 (1994).

15. Zhang I., Sugden K., Williams J. A. R., and Bennion I., "Post fabrication exposure of gap-type bandpass filters in broadly chirped fiber gratings," *Opt. Lett.* **20**(18), 1927–1929 (1995).

16. Sugden K., Zhang L., Williams J. A. R., Fallon L. A., Everall L. A., Chisholm K. E., and Bennion I., "Fabrication and characterization of bandpass filters based on concatenated chirped fiber gratings," *IEEE J. Lightwave Technol.* **15**(8), 1424–1432 (1997).

17. Mizrahi V., Erdogan T., DiGiovanni D. J., Lemaire P. J., MacDonald W. M., Kosinski S. G., Cabot S., and Sipe J. E., "Four channel fibre grating demultiplexer," *Electron. Lett.* **30**(10), 780–781 (1994).

18. Jayaraman V., Cohen D. A., and Coldren L. A., "Demonstration of broadband tunability of a semiconductor laser using sampled gratings," *Appl. Phys. Lett.* **60**(19), 2321–2323 (1992).

19. Leners R., Emplit P., Foursa D., Haelterman M., and Kashyap R., "6.1-GHz dark-soliton generation and propagation by a fiber Bragg grating pulse-shaping technique," *J Opt. Soc. Am. B (Optical Physics)* **14**(9), 2339–2347 (1997).

20. Ibsen M., Durkin Michael K., and Lamming R. I., "Chirped Moiré gratings operating on two-wavelength channels for use as dual-channel dispersion compensators," *IEEE Photon. Technol. Lett.* **10**(1), 84–86 (1998).

21. Huber D. R., "Erbium doped fiber amplifier with a 21 GHz optical filter based on an in-fiber Bragg grating," in *Tech. Digest of ECOC '92,* paper WeP2.2, 473 (1992).

22. Ouellette F., Krug P. A., Stephens T., Doshi G., and Eggleton B., "Broadband and WDM dispersion compensation using chirped sampled fibre Bragg gratings," *Electron. Lett.* **31**(11), 899–901 (1995).

23. Legoubin S., Douay M., Bernage P., and Niay P., "Free spectral range variations of grating-based Fabry–Perot photowritten in optical fibers," *J. Opt. Soc. Am. A* **12**(8), 1687–1694 (1995).

24. Huber D. R., "1.5 μm narrow bandwidth in-fiber gratings," in *Proc. of LEOS '91,* Paper OE3.1 (1991).

25. Morey W. W., Bailey T. J., Glenn W. H., and Meltz G., "Fiber Fabry–Perot interferometer using side exposed fiber Bragg gratings," in *Proc. of OFC '92,* p. 96 (1992).

26. Riant I., Borne S., and Sansonetti P., "Asymmetrical UV-written fibre Fabry–Perot for WDM soliton frequency guiding and equalisation," in *Photosensitivity and Quadratic Nonlinearity in Glass Waveguides: Fundamentals and Applications,* Vol. 22, 1995 OSA Technical Series (Optical Society of America, Washington DC, 1995), pp. SbB4-(18–21) (1995).

27. BT Internal Report, 1993.

28. Town G. E., Sugden K., Williams J. A. R., Bennion I., and Poole S. B., "Wideband Fabry–Perot like filters in optical fibers," *IEEE Photon. Technol. Lett.* **7**(1) (1995).

29. Kashyap R., unpublished.

30. Legoubin S., Fertein E., Douay M., Bermage P., Niay P., Bayon F., and Georges T., "Formation of Moiré gratings in core of germanosilicate fibre by transverse holographic double exposure," *Electron. Lett.* **27**(21) 1945 (1991).

31. Kashyap R., McKee P. F., Campbell R. J., and Williams D. L., "A novel method of writing photo-induced chirped Bragg gratings in optical fibres," *Electron. Lett.* **30**(12), 996–997 (1994).

32. Campbell R. J. and Kashyap R., "Spectral profile and multiplexing of Bragg gratings in photosensitive fibre," *Opts. Lett.* **16**(12), 898–900 (1991).

33. Everall L. A., Sugden K., Williams J. A. R., Bennion I., Liu X., Aitchison J. S., Thom S., and De La Rue R. M., "Fabrication of multi-pass band moiré resonators in fibers by the dual-phase-mask exposure method," *Opt. Lett.* **22**(19), 1473–1475 (1997).

34. Hill K. O., Johnson D. C., Bilodeau F., and Faucher S., "Narrow bandwidth optical waveguide transmission filters," "Electron. Lett. **23**(9), 465–466 (1987).

35. Morey W. W., "Tuneable narrow-line bandpass filter using fibre gratings," in *Proc. Conference on Optical Fiber Communications, OFC '91,* paper PD20-1.

36. Kashyap R. and Nayar B. K., "An all single-mode fibre Michelson interferometer sensor," *IEEE J. Lightwave Technol.* **LT-1**(3), 619–624 (1983).

37. Kogelnik H. and Schmidt R. V., "Switched directional couplers with alternating $\Delta\beta$," *IEEE J. Quantum Electron.* **QE-12**, 396–401 (1976).

38. Digonet M. J. F. and Shaw H. J., "Analysis of a tunable single mode optical fiber coupler," *IEEE J. Quantum Electron.* **QE-18**(4), 746–754 (1982).

39. Snyder A. W., "Coupled mode theory for optical fibers," *J. Opt. Soc. Am.* **62**, 1267–1277 (1972).

40. Nykolak G., de Barros M. R. X., Nielsen T. N., and Eskildsen L., "All-fiber active add-drop wavelength router," *IEEE Photon. Technol. Lett.* **9**(5), 605–606 (1997).

41. Hibino Y., Kitagawa T., Hill K. O., Bilodeau F., Malo B., Albert J., and Johnson D. C., "Wavelength division multiplexer with photoinduced Bragg gratings fabricated in a planar-lightwave-circuit-type asymmetric Mach–Zehnder interferometer," *IEEE Photon. Technol. Lett.* **8**(1), 84–86 (1996).

42. Kashyap R., "A new class of fibre grating based band-pass filters: The highly asymmetric interferometer," *Opt. Commun.* **153**, 14–18 (1998).

43. Bilodeau F., Malo B., Johnson D. C., Albert J., and Hill K. O., "High return loss narrowband all fiber bandpass Bragg transmission filter," *IEEE Photonics Technol. Lett.* **6**(1), 80 (1994).

44. Bilodeau F., Hill K. O., Theriault S., Malo B., Albert J., and Johnson D. C., "Broadband wavelength selective tap using an all fiber Mach-Zehnder interferometer and chirped photo induced Bragg gratings," in *Technical Digest of OFC '96,* paper WF5, p. 119 (1996).

45. Lewis S. A. F., Guy M. J., Taylor J. R., and Kashyap R., "An all fibre periodic spectral filter for the simultaneous generation of WDM channels from broad bandwidth pulsed sources," **34**(12), submitted 1998.

46. Kashyap R., Hornung S., Reeve M. H., and Cassidy S. A., "Temperature desensitisation of delay in optical fibres for sensor applications," *Electron. Lett.* **19**(24), 1039–1040 (1983).

47. Iwashima T., Inoue A., Shigematsu M., Nishimura M., and Hattori Y., "Temperature compensation technique for fibre Bragg gratings using liquid crystalline polymer tubes," *Electron. Lett.* **33**(5), 417–419 (1997).

48. Weidman D. L., Beall G. H., Chyung K. C., Francis G. L., Modavis R. A., and Morena R. M., in *Tech. Digest of ECOC '96,* Vol. 1, Paper MOB.3.5, p. 1.61–64 (1996).

49. Johnson D. C., Hill K. O., Bilodeau F., and Faucher S., "New design configuration for a narrow-band wavelength selective optical tap and combiner," *Electron. Lett.* **23**, 668 (1987).

50. Ragdale C. M., Reid T. J., Reid D. C. J., Carter A. C., and Williams P. J., "Integrated laser and add–drop optical multiplexer for narrowband wavelength division multiplexing," *Electron. Lett.* **28**(8), 712–714 (1992).

51. Maxwell G. D., Kashyap R., and Ainslie B. J., "UV written 1.5 μm reflection filters in single mode planar silica guides," *Electron. Lett.* **28**(22), 2016 (1992).

52. Cullen T. J., Rourke H. N., Chew C. P., Baker S. R., Bircheno T., Byron K., and Fielding A., "Compact all-fibre wavelength drop and insert filter," *Electron. Lett.* **30**(25), 2160–2162 (1994).

53. Kashyap R., Maxwell G. D., and Ainslie B. J., "Laser trimmed four-port bandpass filter fabricated in singlemode planar waveguides," *IEEE Photonics Tech. Lett.* **5**(2) 191 (1993).

54. Kashyap R., Hornung S., Reeve M. H., and Cassidy S. A., "Temperature desensitisation of delay in optical fibres for sensor applications," *Electron. Lett.* **19**(24), 1039–1040 (1983).

55. Kashyap R., Reeve M. H., Cassidy S. A., and Hornung S., "Temperature desensitisation of delay in fibres." UK Patent no. 8328204, 21 Oct. 1983, US Patent no. 4923278, 31 March 1987.

56. Morey W. W. and Glomb W. L., US Patent no. 5042898, 27 August 1991).

57. Mizuochi T. and Kitayama T., "Interferometric cross talk-free optical add/drop multiplexer using cascaded Mach-Zehnder fiber gratings," in *Technical Proc. of OFC '97,* pp. 176–177 (1997).

58. Chawki M. J., Berthou L., Delevaque E., Gay E., and Le Gac I., "Evaluation of an optical boosted add/drop multiplexer OBADM including circulators and fiber grating filters," in *Tech. Digest of ECOC '95,* paper Mo A.3.7 (1995).

59. Huber D. R., "Erbium doped amplifier with a 21 GHz optical filter based on an in-fiber Bragg grating," in *Proc. of ECOC '92,* pp. 473–476 (1992).

60. Delavaque E., Boj S., Bayon J.-F., Poignant H., Le Mellot J., Monerie M., Niay P., and Bernage P., "Optical fiber design for strong grating photo imprinting with radiation mode suppression," in *Proc. of Post-Deadline Papers of OFC '95,* Paper PD5 (1995).

61. Dong L., Reekie L., Cruz J. L., Caplen J. E., and Payne D. N., "Cladding mode suppression in fibre Bragg gratings using fibres with a depressed cladding," in *Tech. Digest of ECOC '96,* Vol. 1, Paper M0B.3.3, pp. 1.53–56 (1996).

62. Goldstein E. L., "Performance implications of crosstalk in transparent lightwave networks," *IEEE Photon. Technol. Lett.* **6**(5), 657 (1994).

63. Eggleton B. J., Lenz G., Litchinitser N., Patterson D. B., and Slusher R. E., "Implications of fiber grating dispersion for WDM communication systems," *IEEE Photon. Technol. Lett.* **9**, 1403–1405 (1997).

64. Okayama H., Ozeki Y., and Kunii T., "Dynamic wavelength selective add/drop node comprising tunable gratings," *Electron. Lett.* **33**(10), 881–882 (1997).

65. Quetel L., Rivollan L., Delevaque E., Gay E., and Le Gac I., "Programmable fibre grating based wavelength demultiplexer," in *Tech. Digest of OFC '96,* Paper WF6 (1996).

66. Kim S. Y., Lee S. B., Kwon S. W., Choi S. S., and Jeong J., "Channel-switching active add/drop multiplexer with tunable gratings," *Electron. Lett.* **34**(1), 104–105 (1998).

67. Okayama H., Ozeki Y., Kamijoh T., Xu C. Q., and Asabayashi I., "Dynamic wavelength selective add/drop node comprising fibre gratings and switches," *Electron. Lett.* **33**(5), 403–404 (1997).

68. Ellis A. D., Kashyap R., Crisp I., Malyon D. J., and Hueting, J. P., "Demonstration of an 80 Gb/s throughput, reconfigurable dispersion compensating WDM ADM using Deuterium sensitised 10 cm stop chirped fibre Bragg gratings," in *Proc. of ECOC '97,* Vol. 1, pp. 171–175 (1997).

69. Bircheno T. and Baker V., "A fibre polarisation splitter/combiner," *Electron. Lett.* **21**(6), 2521–2522 (1985).

70. Lefevre H. C., "Single-mode fibre fractional wave devices and polarisation controllers," *Electron. Lett.* **16**, 778–780 (1980).

71. Guy M. J., Chernikov S. V., Taylor J. R., and Kashyap R., "Low loss fibre Bragg grating transmission filter based on a fiber polarization splitter," *Electron. Lett.* **30**(18), 1512–1513 (1994).

72. Chernikov S. V., Taylor J. R., and Kashyap R., "All-fiber dispersive transmission filters based on fiber grating reflectors," *Opt. Lett.* **20**(14), 1586–1588 (1995).

73. Kim S. Y., Lee S. B., Chung J., Kim S. Y., Park I. J., Jeong J., and Choi S. S., "Highly stable optical add/drop multiplexer using polarization beam splitters and fiber Bragg gratings," *IEEE Photon. Technol. Lett.* **9**(8), 1119–1121 (1997).

74. Taylor H. F., "Frequency selective coupling in parallel dielectric waveguides," *Opt. Commun.* **8**, 423 (1973).

75. Elachi C. and Yeh P., "Frequency selective coupler for integrated optic systems," *Opt. Commun.* **7**, 201 (1973).

76. Baumann I., Seifert J., Nowak W., and Sauer M., Compact all-fiber add–drop multiplexer using fiber Bragg gratings," *IEEE Photon. Technol. Lett.* **8**(10), 1331–1333 (1997).

77. Orlov S. S., Yariv A., and Van Essen S., "Coupled mode analysis of fiber optic add–drop filters for dense wavelength division multiplexing," *Opt. Lett.* **22**(10), 688–690 (1997).

78. Kewitsch A. S., Rakuljic G. A., Willems P. A., and Yariv A., "An all-fiber, zero insertion loss add/drop filter for wavelength division multiplexing," in *Bragg Gratings, Photosensitivity, and Poling in Glass Fibers and Waveguides: Applications and Fundamentals,* Vol. 17, OSA Technical Digest Series (Optical Society of America, Washington DC, 1997), paper BTuA2, pp. 256–258.

79. Kashyap R., "A simplified approach to Bragg grating based Michelson and the in-coupler Bragg grating add-drop multiplexers," in *Tech. Digest of OFC '99,* paper TuN3, 1999.

80. Yariv A. and Yeh P., *Optical Waves in Crystals,* Chapter 6. Wiley, New York (1984).

81. Syms R. R. A., "Optical directional coupler with a grating overlay," *Appl. Opt.* **24**(5), 717–726 (1985).

82. Archambault J.-L., Ph.D. Thesis, University of Southampton (1994).

83. Archambault J.-L., Russell P. St. J., Barcelos S., Hua P., and Reekie L., "Grating frustrated coupler: a novel channel-dropping filter in single-mode optical fiber," *Opt. Lett.* **19**(3), 180–182 (1994).

84. Wolting S., "Grating frustrated couplers," BT Research Laboratories Summer Studentship Report (1995).

85. Kashyap R., Wyatt R., and McKee P. F., "Wavelength flattened saturated erbium amplifier using multiple side-tap Bragg gratings," *Electron. Lett.* **29**(11), 1025 (1993).

86. Vengsarkar A. M., Pedrazzani J. R., Judkins J. B., Lemaire P. J., Bergano N. S., and Davidson C. R., "Long-period fiber grating based gain equalisers," *Opt. Lett.* **21**, 336–338 (1996).

87. Stegull D. B. and Erdogan T., "Long-period fiber-grating devices based on leaky cladding mode coupling," in *Bragg Gratings, Photosensitivity, and Poling in Glass Fibers and Waveguides: Applications and Fundamentals,* Vol. 17, OSA Technical Digest Series (Optical Society of America, Washington DC, 1997), paper BTuA2, pp. 16–18.

88. Wagener J. L., Strasser T. A., Pedrazzani J. R., and DeMarco J., "Fiber grating optical spectrum analyser tap," in *Tech. Digest of ECOC '97, Publn. No. 448,* pp. 65–68.

89. Bardal S., Kamal A., and Russell P. St. J., "Photoinduced birefringence in optical fibres: a comparative study of low-birefringence and high-birefringence fibers," *Opt. Lett.* **17**(6), 411 (1992).

90. Russell P. St. J. and Hand D. P., "Rocking filter formation in photosensitive high birefringence optical fibres," *Electron. Lett.* **26**, 1846–1848 (1990).

91. Kanellopoulos S. E., Valente L. C. G., Handerek V. A., and Rogers A. J., "Comparison of photorefractive effects and photogenerated components in polarisation maintaining fibres," *SPIE* **1516**. "International Workshop on Photo-induced Self-Organisation effects in Optical Fibres," p. 200 (1991).

92. An S. and Sipe J. E., "Polarisation aspects of two-photon photosensitivity in birefringent optical fibers," *Opt. Lett.* **17**(7) (1992).

93. Handerek V. A., Kanellopoulos S. E., Jamshidi H., and Rogers A. J., "Simultaneous observation of photobleaching and photorefractive effects in germanium-doped optical fibers," *Photon. Technol. Lett.* **3**(3), 244–246 (1991).

94. Ouellette F., Gagnon D., and Porier M., "Permanent birefringence in Ge-doped fiber," *Appl. Phys. Lett.* **58**(17), 1813 (1991).

95. Poirier M., Thibault S., Lauzon J., and Ouellette F., "Dynamic and orientational behaviour of UV induced luminescence bleaching in Ge-doped silica optical fiber," *Opt. Lett.* **18**(11), 870 (1993).

96. Parent M., Bures J., Lacroix S., and Lapierre J., "Propriétés de polarisation des réflecterus de Bragg induits par photosensibilité dans les fibres optiques monomode," *Appl. Opt.* **24**(3), 354 (1985).

97. Ouellette F., Gagnon D., and Porier M., "Permanent birefringence in Ge-doped fiber," *Appl. Phys. Lett.* **58**(17), 1813 (1991).

98. Lauzon J., Gagnon D., LaRochelle S., Boulin F., and Ouellette F., "Dynamic polarization coupling in elliptical-core photosensitive fiber," *Opt. Lett.* **17**, 1664 (1992).

99. Kamal A., Kanellopoulos S. E., Archambault J.-L., Russell P. St. J., Handerek V. A., and Rogers A. J., "Holographically written reflective polarization filter in single-mode optical fibers," *Opt. Lett.* **17**(17), 1189–1191 (1991).

100. Wong D., Poole S. B., and Skeats M. G., "Stress-birefringence reduction in elliptical-core fibres under ultraviolet irradiation," *Opt. Lett.* **17**(24), 1773 (1992).

101. Hill K. O., Bilodeau F., Malo B., and Johnson D. C., "Birefringent photosensitivity in monomode optical fibre: application to external writing of rocking filters," *Electron. Lett.* **27**(17), 1548 (1991).

102. Johnson D. C., Bilodeau F., Malo B., Hill K. O., Wigley P. G. J., and Stegeman G. I., "Long length, long-period rocking filters fabricated from conventional monomode telecommunications optical fibres," *Opt. Lett.* **17**(22), 1635 (1992).

103. Malo B., Bilodeau F., Johnson D. C., and Hill K. O., "Title of ARTICLE," in *Optical Fiber Communication Conf.*, Vol. 5 of 1992 OSA Tech. Digest. Series (Optical Society of America, Washington D.C., 1992), paper PD23, p. 404, 1992.

104. Lefevre H. C., "Single-mode fibre fractional wave devices and polarisation controllers," *Electron. Lett.* **16**, 778–780 (1980).

105. Psaila D. C., de Sterke M., and Ouellette F., "Double pass technique for fabricating compact optical fibre rocking filters," *Electron. Lett.* **31**(13), 1093–1094 (1995).

106. Kannellopoulos S. E., Handerek V. A., and Rogers A. J., "Compact Mach–Zehnder fibre interferometer incorporating photo-induced gratings in elliptical core fibres," *Opt. Lett.* **18**(12), 1013–1015 (1995).

107. Park H. G. and Kim B. Y., "Intermodal coupler using permanently photoinduced grating in two mode optical fibre," *Electron. Lett.* **25**(12), 797 (1989).

108. Ouellette F., "Phase-matching of optical fibre photosensitive intermodal couplers in infra-red," *Electron. Lett.* **25**(23), 1590–1591 (1989).

109. Vengsarkar A. M., Greene J. A., and Murphy K. A., "Photoinduced refractive index changes in two-mode elliptical core fibers: sensing applications," *Opt. Lett.* **16**(19), 1541–1543 (1991).

110. Park H. G., Huang S. Y., and Kim B. Y., "All-optical intermodal switch using periodic coupling in a two-mode waveguide," *Opt. Lett.* **14**(16), 877–879 (1989).

111. Blake J. N., Huang S. Y., Kim B. Y., and Shaw. H. J., "Strain effects on lightly elliptical core two mode fibers," *Opt. Lett.* **12**, 732 (1987).

112. Ouellette F., "Theoretical aspects of intermodal couplers in photosensitive optical fibers," in *Tech. Digest of Integrated Photonics Research*, 1990, p. 96.

113. K. O., Malo B., Vineberg K. A., Bilodeau F., Johnson D. C., and Skinner I., "Efficient mode conversion in telecommunication fibre using externally written gratings," *Electron. Lett.* **26**(16), 1270 (1990).

114. Morey W. W., Meltz G., Love J. D., and Hewlett S. J., "Mode-coupling characteristics of photo-induced Bragg gratings in depressed cladding fiber," *Electron. Lett.* **30**, 730–731 (1994).

115. Johlen D., Klose P., Renner H., and Brinkmeyer E., "Strong LP_{11} mode splitting in UV side written tilted gratings," in *Bragg Gratings, Photosensitivity, and Poling in Glass Fibers and Waveguides: Applications and Fundamentals*, Vol. 17, OSA Technical Digest Series (Optical Society of America, Washington, DC, 1997), Paper BMG12, pp. 219–221.

116. Haggans C. W., Singh H., Varmer W. F., and Wang J.-S., "Analysis of narrow-depressed cladding fibers for minimization of cladding mode losses in fiber Bragg gratings," in *Bragg Gratings, Photosensitivity, and Poling in Glass Fibers and Waveguides: Applications and Fundamentals*, Vol. 17, OSA Technical Digest Series (Optical Society of America, Washington, DC, 1997), Paper BMG11, pp. 217–218.

117. Shi C.-X. and Okoshi T., "Analysis of a fiber $LP^{02} \leftrightarrow LP^{02}$ mode converter," *Opt. Lett.* **17**, 719 (1992).

118. Bilodeau F., Hill K. O., Malo B., Johnson D. C., and Skinner I. M., "Efficient, narrowband $LP_{01} \leftrightarrow LP_{02}$ mode converters fabricated in photosensitive fiber: Spectral response," *Electron. Lett.* **27**, 682–682 (1991).

119. Ky N. H., Limberger H. G., and Salathé R., "Efficient broadband intracore grating LP_{01}–LP_{01} mode converters for chromatic dispersion compensation," *Opt. Lett.* **23**(6), 445–447 (1998).

120. Kashyap R., McKee P. F., Campbell R. J., and Williams D. L., "A novel method of writing photo-induced chirped Bragg gratings in optical fibres," *Electron. Lett.* **30**(12), 996–997 (1994).

This page intentionally left blank